

Efficient green hydrogen production through metal-organic framework-derived Ni and Co mediated iron selenide hexagonal nanorods and wireless coupled with photovoltaics for urea and alkaline water electrolysis

Mikiyas Mekete Meshesha ^{a,b}, Debabrata Chanda ^{a,b}, Ranjith Balu ^{a,b}, Seok Gwon Jang ^{a,b}, Shahbaz Ahmed ^{a,b}, Bee Lyong Yang ^{a,b,*}

^a School of Advanced Materials Science and Engineering, Kumoh National Institute of Technology, 61 Daehak-ro, Gumi-si, Gyeongbuk 39177, Republic of Korea
^b GHS Co. Ltd., Gumi-Si, Republic of Korea

ARTICLE INFO

Keywords:
 Bifunctional catalyst
 Electrocatalyst
 Water splitting
 Urea electrolysis
 Photovoltaics-electrochemical
 AEMWE

ABSTRACT

Metal-organic framework (MOF)-based catalysts are gaining attention due to their tunable properties. In this study, we synthesized MOF based Ni and Co doped iron selenide (NiCoFeSe) hexagonal nanorods electrocatalyst. This NiCoFeSe catalyst exhibited outstanding performance in the hydrogen evolution reaction (HER), oxygen evolution reaction (OER), and urea oxidation reaction (UOR) with impressively low overpotentials of 220, 275 mV for HER, 230, 330 mV for OER, and 210, 300 mV for UOR at current densities of 50 and 100 μ Acm $^{-2}$, respectively. Additionally, we fabricate a wireless flexible and rigid photovoltaic-electrochemical device utilizing NiCoFeSe as both the anode and cathode, achieving an impressive solar-to-hydrogen efficiency of 11.1%. Furthermore, we developed an anion exchange membrane water electrolyzer with NiCoFeSe as anode and cathode, achieving a current density of 1.07 μ Acm $^{-2}$ at 1.85 V, along with a cell efficiency of 69.67% and an energy consumption of 47.85 kWh to produce 1 kg of hydrogen.

1. Introduction

The hydrogen fuel is a promising green and environmental-friendly energy source [1]. Among hydrogen generation methods, electrochemical water splitting (EWS) using renewable energy source is backbone technology for production of pure hydrogen and sufficient amount [2]. EWS consists of two electrochemical reaction components, these are hydrogen evolution reaction (HER) and oxygen evolution reaction (OER). The efficiency of EWS is limited due to the low reaction rates of HER and OER [3–9]. Therefore, catalysts should be employed to speed up these low reaction rates to improve the efficiency EWS. Precious-metal materials, Pt as HER and RuO₂ as OER, are excellent electrocatalysts. While noble materials have shown excellent potential for EWS applications, their high cost, scarcity, and limited durability pose challenges for large-scale industrial implementation [10]. Consequently, there is a pressing need to identify alternative candidates that can address these issues and offer a more viable solution. The quest for

alternative catalyst materials is driven by the pursuit of cost-effective and readily available elements that can match or even surpass the performance of noble materials. Additionally, these alternatives must demonstrate long-term stability and durability when subjected to the rigorous conditions of water splitting processes. By exploring such alternative candidates, we can overcome the limitations associated with noble materials and pave the way for practical and economically feasible water splitting technologies.

Extensive research efforts have been directed towards the development and characterization of novel catalysts, including earth-abundant metal-based compounds, transition metal oxides, sulfides, selenides and phosphides, as well as various hybrid and composite materials [11–28]. These substitute catalysts carry significant potential in realizing efficient and sustainable water splitting, striking a balance between performance, cost-effectiveness, and widespread availability. Concentrating on the exploration and enhancement of these alternative catalysts enables us to tackle the challenges linked to noble materials

* Corresponding author at: School of Advanced Materials Science and Engineering, Kumoh National Institute of Technology, 61 Daehak-ro, Gumi-si, Gyeongbuk 39177, Republic of Korea.

E-mail address: blyang@kumoh.ac.kr (B.L. Yang).



and expedite the shift towards extensive industrial adoption of water splitting technologies. This research direction is crucial for advancing the field of electrocatalysis and facilitating the widespread adoption of water splitting as a viable method for clean hydrogen production. In addition, Metal-organic framework (MOF) derived catalysts have emerged as highly promising candidates for electrochemical water splitting (EWS) applications [29–35]. This is primarily due to their unique structural characteristics, including a large surface area, well-defined pore structure, presence of metal active sites, and channel-based architecture. Besides, modulating the composition of MOF through heteroatom doping represents a promising strategy for developing efficient bifunctional electrocatalysts for water splitting. The incorporation of heteroatoms can fine-tune the electronic structure of MOF, optimize adsorption energies of reactive species in water splitting reactions, create defects and distortions in the lattice, and increase the number of catalytically active sites [36,37]. This approach enables the development of bifunctional catalysts with superior water splitting performance. Felix et al. report cobalt-iron selenide which has an overpotential of 270 mV at a current density of 10 mA cm^{-2} with Tafel slope of 78 mV dec^{-1} [38]. Shan Ni et al. successfully synthesized $\text{NiSe}_2/\text{FeSe}_2$ electrode, achieving an overpotential of 256 mV at a current density of 10 mA cm^{-2} [39]. Hence, doping of transition metals improved intrinsic conductivity and reduced ΔG^* by optimizing the electronic structure of the catalyst, thereby enhancing HER performance. The improved OER activity was attributed to the generation of high-valence-state species under anodic potentials in alkaline solutions.

Based on above motivation, we have synthesized nickel and cobalt doped iron selenide (NiCoFeSe) hexagonal nanorods using hydrothermal synthesis method, with the material being derived from a MOF. The resulting material shows promise for use in bifunctional water splitting. Bimetallic doping enhances the catalytic activity of iron selenide towards both the HER and OER, which are the two half-reactions involved in water splitting. This means that NiCoFeSe can function as a bifunctional catalyst, which is desirable for efficient and cost-effective water splitting. The hexagonal crystal structure of NiCoFeSe provides a high surface area, which can increase the active sites available for catalysis and improve the overall efficiency of the material. The NiCoFeSe catalyst has exhibited outstanding performance in a wide range of electrochemical reactions, including HER, OER, and UOR. Notably, this catalyst boasts remarkable attributes, characterized by impressively low overpotentials at both 50 mAc m^{-2} and 100 mAc m^{-2} current densities. Specifically, it achieves overpotentials of 220 mV and 275 mV for HER, 230 mV and 330 mV for OER, and 210 mV and 300 mV for UOR, respectively and low activation energy of $16.23 \text{ kJ mol}^{-1}$. NiCoFeSe has good stability and durability under electrochemical conditions for 200 h, which is important for practical applications of water splitting technologies. Beyond its impressive electrochemical properties, this versatile catalyst has found successful applications in the development of wireless flexible and rigid photovoltaic-electrochemical devices. These devices have achieved an impressive solar-to-hydrogen efficiency rate of 11.1%, showcasing the catalyst's potential for sustainable energy conversion. Moreover, the NiCoFeSe catalyst has proven to be highly effective in anion exchange membrane water electrolysis. In this context, it has delivered remarkable outcomes, including a notable current density of 1.07 Acm^{-2} at a low voltage of 1.85 V. Additionally, the cell efficiency reached an impressive 69.67%, while the energy consumption for producing 1 kg of hydrogen was a commendably low 47.85 kWh. These results underscore the catalyst's significance in advancing the field of clean and efficient hydrogen production.

2. Experiment details

2.1. Materials

Iron nitrate ($\text{Fe}(\text{NO}_3)_3 \cdot 9 \text{ H}_2\text{O}$), cobalt nitrate ($\text{Co}(\text{NO}_3)_2 \cdot 6 \text{ H}_2\text{O}$, 97%), $\text{Ni}(\text{NO}_3)_3 \cdot 6\text{H}_2\text{O}$, dimethylformamide (DMF), fumaric acid,

commercial Pt/C (20.0 wt%), Nafion (5.0 wt%), ruthenium oxide (RuO_2 , 99.9%), ethanol ($\text{C}_2\text{H}_5\text{OH}$, 99.9%), methanol (CH_3OH , 99.9%), copper tape, hydrochloric acid (HCl, (35–37%), potassium hydroxide (KOH, $\geq 99.5\%$), Ni fiber paper (NFP), SustainionTM X37–50 RT membrane, and SustainionTM XC-1 and nickel mesh (NM) substrate were purchased from Sigma Aldrich.

2.2. Preparation of catalyst

2.2.1. Synthesis of MIL-88A metal-organic frameworks (MOFs)

In a typical procedure, a combination of 300 mg $\text{Fe}(\text{NO}_3)_3 \cdot 9 \text{ H}_2\text{O}$ and 150 mg fumaric acid was blended in a mixture of 20 mL DMF and 4 mL H_2O . This mixture was allowed to react for a duration of 72 h, resulting in the formation of a solution with red-yellow hues. The resulting solution was subsequently transferred to a Teflon-lined stainless-steel autoclave with a 60 mL capacity. A hydrothermal reaction was carried out within this autoclave at a temperature of 115 °C for a period of 7 h. Following the reaction, the precipitate was gathered through centrifugation, then subjected to a thorough washing process using water and ethanol, repeatedly. Finally, the collected precipitate was dried at 70 °C for a duration of 12 h.

2.2.2. Synthesis of FeSe hexagonal nanorods

A solution is prepared from MIL-88A (14 mg) and 20 mL DMF. Then, the mixture was introduced into a solution containing sodium borohydride and selenide powder. Subsequently, a hydrothermal synthesis procedure was executed at a temperature of 190 °C for a duration of 14 h, which led to the creation of FeSe . The produced FeSe underwent multiple purification rounds using purified water and ethanol, followed by a dehydration process at 70 °C for 12 h, resulting in the production of a dry product.

2.2.3. Synthesis of CoFeSe hexagonal nanorods

The initial step involved the dispersion of MIL-88A (14 mg) in 20 mL of DMF, resulting in the formulation of solution 1. In parallel, solution 2 from urea and $\text{Co}(\text{NO}_3)_2 \cdot 6 \text{ H}_2\text{O}$ were dissolved in 25 mL of water. By blending solutions 1 and 2, solution 3 prepared and underwent a heating process at 110 °C for a period of 8 h within a fully sealed Teflon-lined stainless-steel autoclave, having a capacity of 60 mL. Following the reaction, added into a solution containing sodium borohydride, and selenide powder. Subsequently, a hydrothermal synthesis process was carried out at a temperature of 190 °C for a duration of 14 h, resulting in the formation of a CoFeSe . The synthesized CoFeSe cleaned multiple rounds of purification using purified water and ethanol, followed by dehydration at 70 °C for 12 h to yield a dry product.

2.2.4. Synthesis of NiFeSe hexagonal nanorods

The process commenced with the dispersion of MIL-88A (14 mg) in 20 mL of DMF, assign as solution 1. Concurrently, solution 2 is prepared from urea and $\text{Ni}(\text{NO}_3)_3 \cdot 6 \text{ H}_2\text{O}$ dissolved in 25 mL of water. Through the mixture of solutions 1 and 2, the solution 3 prepared. This solution 3, hydrothermally heated at 110 °C for a span of 8 h within a sealed Teflon-lined stainless-steel autoclave, with a volumetric capacity of 60 mL. After the reaction, we introduced the result into a solution containing sodium borohydride and selenide powder. Following this, we conducted a hydrothermal synthesis process at a temperature of 190 °C, allowing it to proceed for 14 h. This led to the formation of NiFeSe . Subsequently, the synthesized CoFeSe nanorods washed multiple rounds of purification using purified water and ethanol. Finally, they were dehydrated at 70 °C for 12 h to obtain a dry product.

2.2.5. Synthesis of NiCoFeSe hexagonal nanorods

To start, MIL-88A (14 mg) in 20 mL of DMF were dissolved in through stirring at room temperature. In a separate solution, 150 mg of $\text{Co}(\text{NO}_3)_3 \cdot 3 \text{ H}_2\text{O}$ a variable amount of $\text{Ni}(\text{NO}_3)_3 \cdot 6 \text{ H}_2\text{O}$ (50–200 mg), and urea were combined with 25 mL of water. These solutions were

thoroughly mixed and then transferred into a 60 mL Teflon-lined stainless autoclave. A hydrothermal reaction was carried out at 110 °C for 6 h. Subsequently, introduced into a solution containing sodium borohydride and selenide powder in order to selenization, followed by subjecting the mixture to a hydrothermal synthesis process at 190 °C for a span of 14 h. This procedure culminated in the creation of a hexagonal nanorod structure assigned as NiCoFeSe. The synthesized NiCoFeSe nanorods underwent several cycles of purification utilizing purified water and ethanol, followed by a dehydration step at 60 °C for 12 h, yielding the final dried product.

2.3. Setting up and operating an alkaline water electrolyzer

2.3.1. Two electrode alkaline electrolyzer

The two-electrode single-chamber configuration is a commonly used setup in water electrolysis research. It simplifies the system by having both the anode and cathode in the same chamber, which can be advantageous for certain applications. This design reduces the complexity of the electrolyzer, potentially making it more cost-effective and easier to scale up for industrial applications. By using NiCoFeSe for both the anode and cathode, the researchers aim to maximize the efficiency of the electrolyzer and potentially improve its overall performance.

2.3.2. Cleaning and pretreatment of nickel fiber paper electrodes

Activated nickel fiber paper (NFP) was utilized both as anodes and cathodes to enhance gas diffusion during electrochemical reactions. We used commercially available NFP sheets for this purpose. To prepare the NFP pieces, they were immersed in a 0.2 M HCl solution. An ultrasonic treatment lasting 20 min was employed to facilitate the cleaning and activation of the NFP material. After the ultrasonication process, the NFP sections underwent a thorough rinsing with deionized water to eliminate any remaining acid and impurities. Following this step, the NFP pieces were further rinsed with ethanol to ensure the complete removal of any lingering contaminants. Subsequently, the cleaned NFP electrodes were dried in an oven set at 70 °C for a duration of 5 h.

2.3.3. Preparing gas diffusion electrodes (GDL)

The fabrication process for the anode and cathode electrodes involved a coating technique. To create these electrodes, a catalyst (40 mg) was mixed with a solution comprising water (10 mL), ethanol (4 mL), and a binder (200 µL). This mixture was subjected to ultrasonication for a duration of 1 h. The resulting catalytic ink had a loading of approximately 2.5 mg cm⁻² for both the anode and cathode. Subsequently, the uniform catalyst ink was applied to Nickel Fiber Paper Gas Diffusion Layers (NFP GDL) using the spray coating method. As a point of reference for comparison, the anode was constructed using RuO₂-coated NFP. Similarly, the cathode was prepared using 20% Pt/C-coated NFP.

2.3.4. PV-EC alkaline water electrolysis

In our PV system fabrication process, we utilized a laser machine to precision-cut the solar cells into the desired sizes. Following the cutting process, thorough cleaning of the cell surfaces was performed, and series connections were established for assembly. To evaluate the performance of the solar cells, we conducted I-V (current-voltage) curve measurements utilizing a Keithley instrument. These measurements were conducted under simulated AM 1.5 G light conditions, which provided an irradiance of 100 mW cm⁻². We have successfully created two distinct photovoltaic devices: one with a rigid configuration and the other featuring flexibility. The rigid system boasts a rigid structure, while the flexible device offers versatility in its shape, accommodating circular, semi-circular, or flat configurations. In the final step of our process, we established connections between the photovoltaic (PV) device, the cathode, and the anode, eliminating the need for external wiring. For these connections, we employed NiCoFeSe as both the anode and cathode materials. This experimental setup and choice of materials

demonstrate a systematic approach to evaluating the performance of a conventional water electrolyzer. The study's findings could have implications for the development of more efficient and cost-effective hydrogen production technologies, which are essential for the advancement of clean energy solutions.

2.3.5. Zero-gap alkaline water electrolyzer

In our study on water electrolysis, we utilized an anion-exchange membrane as the solid polymer matrix. Before commencing the electrolysis process, it was imperative to activate the membrane in order to remove water-soluble substances from its structure and initiate the ion-exchange particles. To create the membrane electrode assembly (MEA), we employed a method where we placed an anion-exchange membrane, specifically Sustainion™ X37-50 RT, between two NiCoFeSe/NEP electrodes, which served as both the cathode and anode. This assembly was achieved using a hot press technique at a temperature of 50 °C and a pressure of 1.8 MPa. The resulting single anion-exchange membrane water electrolyzer (AEMWE) cell was operated at a temperature of 50 °C while immersed in a 1 M KOH aqueous medium. To evaluate the stability of the electrolyzer's performance, we conducted a series of tests under AEMWE conditions, maintaining a constant applied potential throughout the experiments. For the purpose of comparative analysis, we also designed and tested MEAs that featured a Pt/C/NF cathode and a RuO₂/NF anode. These MEAs underwent experimentation under conditions that closely resembled those of the AEMWE setup.

3. Results and discussion

3.1. Morphology and phase analysis

In Fig. 1a, the various steps involved in the synthesis of NiCoFeSe are illustrated. The process begins with the fabrication of NiCoFe through a hydrothermal method using fumaric acid, iron nitrate, nickel nitrate, cobalt nitrate and urea. The determination of the optimal doping amount is assessed through LSV, as illustrated in Fig. S1a. Subsequently, a selenization step is carried out, resulting in the formation of NiCoFeSe.

To investigate the morphology and structural behavior of the synthesized catalysts, field-emission scanning electron microscopy (FE-SEM) was conducted. The material known as NiCoFeSe exhibits a specific physical shape and structure referred to as a hexagonal nanorod, as shown in Fig. 1b-c. This morphology indicates that the NiCoFeSe material possesses a hexagonal shape resembling a six-sided polygon and is composed of small rod-like structures at the nanoscale. The surface of NiCoFeSe appears to be rough. This means that the outer layer or surface of the NiCoFeSe material displays a more uneven and irregular texture. The synthesis process of NiCoFeSe has yielded a well-formed structure, implying that it has been effectively produced. This suggests that the desired morphology of NiCoFeSe, with its hexagonal nanorod shape, has been successfully achieved through the synthesis procedure. Hexagonal nanorods have shown promise in water splitting applications due to their unique structural and chemical properties. Hexagonal nanorods typically have a high aspect ratio, meaning they have a large surface area compared to their volume [38–41]. This increased surface area provides more active sites for chemical reactions, enhancing the efficiency of water splitting. Moreover, the hexagonal shape of the nanorods offers anisotropic properties, meaning they exhibit different physical and chemical characteristics along different crystallographic directions. This anisotropy allows for preferential exposure of certain crystal facets, which can have different catalytic activities [39–45]. It has been observed that specific crystal facets of hexagonal nanorods can be more favorable for the water splitting reaction, leading to improved performance. In addition, the elemental composition and distribution of the NiCoFeSe catalyst were examined using EDS analysis. The results, presented in Fig. 1d, demonstrate the uniform and even distribution of Ni, Co, Fe, and Se throughout the catalyst material. EDS analysis provides valuable insights into the elemental makeup and spatial distribution of

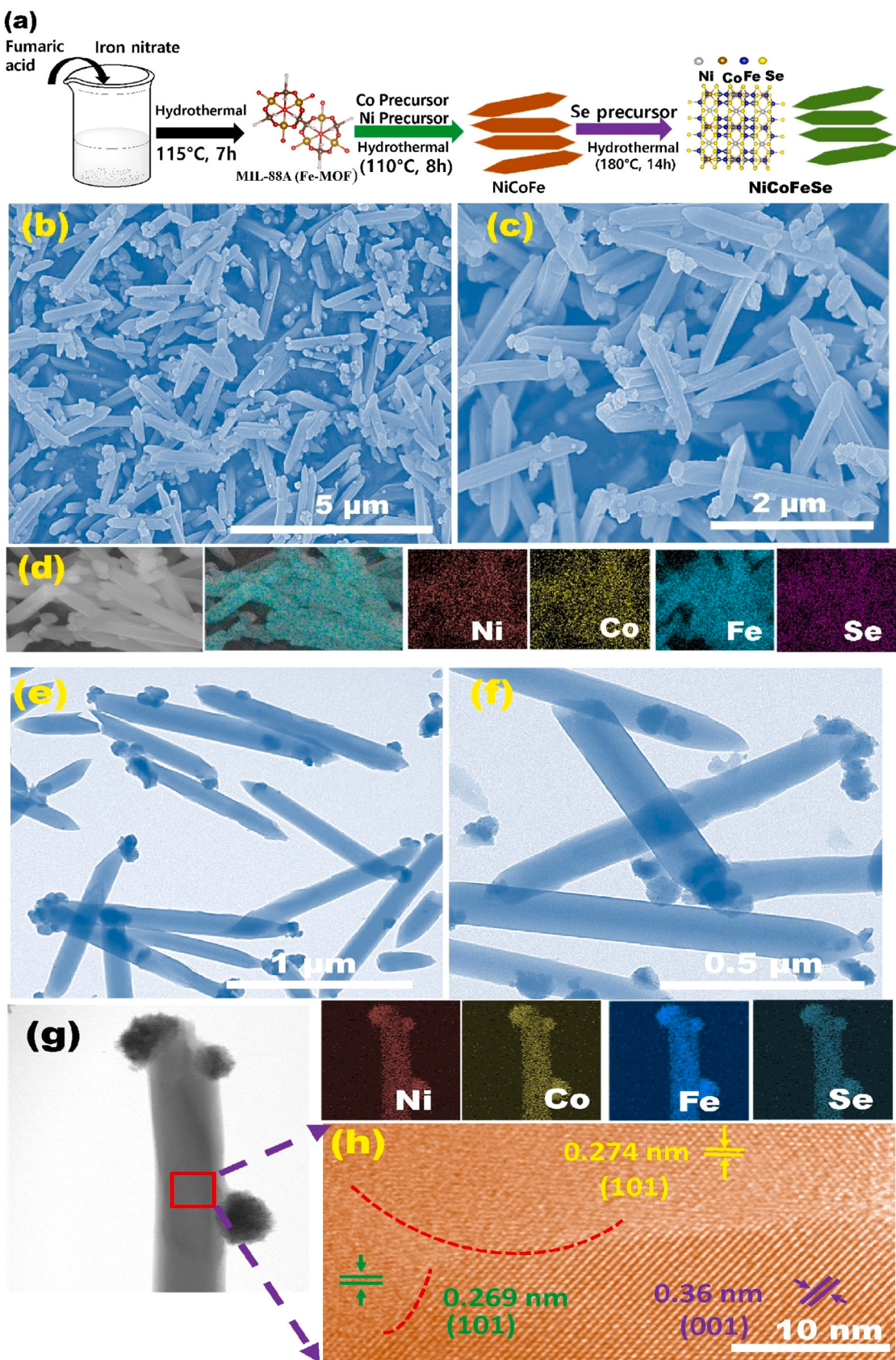


Fig. 1. (a) Synthesis Route for NiCoFeSe, (b-c) FE-SEM image for NiCoFeSe, (d) EDS analysis of NiCoFeSe, (e-f) FE-TEM for NiCoFeSe (g) EDS analysis NiCoFeSe, (h) HR-TEM.

the catalyst. In this case, the results indicate that Ni, Co, Fe, and Se are evenly dispersed within the catalyst, suggesting a homogeneous composition. This uniform distribution is desirable as it promotes efficient catalytic activity and ensures consistent performance across the catalyst's surface. The EDS analysis findings reinforce the potential of the NiCoFeSe catalyst for applications such as water splitting. By confirming the uniform presence of the key elements, the study provides further support for the catalyst's suitability and effectiveness in facilitating important chemical reactions [45–49].

The morphology and structural properties of synthesized catalysts are also investigated using field-emission transmission electron microscopy (FE-TEM). The FE-TEM analysis (Fig. 1e-f) unveils the existence of hexagonal nanorods in NiCoFeSe. This characterization provides valuable insights into the physical shape and arrangement of the catalyst, indicating specific crystallographic orientations and surface facets that can greatly influence its performance. The hexagonal nanorod structure suggests a high surface area, leading to enhanced catalytic activity and potential suitability for various applications. Understanding the morphology and structure of NiCoFeSe catalysts through FE-TEM analysis is crucial for optimizing their design, improving catalytic efficiency, and unlocking their potential for use in sustainable energy conversion, environmental remediation, and other chemical processes. Furthermore, the elemental placement was analyzed using EDS, which revealed the presence and uniform dispersion of Ni, Co, Fe, and Se, as depicted in Fig. 1g. Lastly, the HR-TEM analysis provided valuable insights. The results we acquired revealed a unique signature characterized by dimensions of 0.360 nm, 0.274 nm, and 0.269 nm, corresponding to the crystallographic planes (001), (101), and (101), respectively. These dimensions are associated with iron selenide, nickel selenide, and cobalt selenide, as depicted in Fig. 1h. This observation further supports the understanding of the microstructural characteristics and behavior of the material.

The morphology and structural characteristics of the prepared catalysts are further examined through in-situ transmission electron microscopy (in-situ TEM). The in-situ TEM results are depicted in Fig. S10, showcasing observations at both 1200 s and 3600 s. These findings substantiate the durability of NiCoFeSe, as they reveal a consistent structure and morphology over the specified time interval.

The crystalline nature of our synthesized material was also investigated using X-ray diffraction (XRD) measurements. The XRD pattern of the as-synthesized MIL-88A, as shown in Supplementary Fig S2a, exhibits diffraction peaks that are in full agreement with those previously reported for MIL-88A (Fe) [50,51]. In Fig. 2a, the XRD spectra of FeSe, NiFeSe, CoFeSe, and NiCoFeSe samples are presented. The XRD analysis of FeSe reveals distinct peak patterns at 29.7°, 36.3°, 43.6°, 55.2°, and 63.4°. These well-defined peaks correspond to the crystallographic planes (011), (120), (121), (031), and (122) of the iron selenide phase, respectively. The identification of this phase has been verified by comparing it with the JCPDS 85–0735 database [52,53], which serves as a reliable reference for crystallographic data. Furthermore, the pattern of NiFeSe reveals supplementary peaks at 38.7°, 48.3°, and 53.5°, which can be attributed to the presence of nickel selenide alongside the FeSe peaks. This identification is consistent with the data in the JCPDS 75–0610 database [54,55], further supporting the characterization of the sample's composition. Additionally, there is a noticeable shift in the peak at 29.7°, a result of the nickel doping, accompanied by a slight decrease in peak intensity. Additionally, the XRD pattern for CoFeSe reveals peaks at 33.3°, 44.1°, and 50.1°, in conjunction with the FeSe peaks, indicating the presence of cobalt selenide in the sample. These findings are consistent with the crystallographic data for cobalt selenide found in the JCPDS 70–2870 database [56,57]. Additionally, there is a noticeable shift in the FeSe peak at 64.7°, attributable to cobalt doping, accompanied by a reduction in peak intensity. In conclusion, the XRD pattern of NiCoFeSe exhibits distinct peaks associated with iron selenide, cobalt selenide, and nickel selenide, as illustrated in Fig. 2a. When compared to the XRD patterns of FeSe, NiFeSe, and CoFeSe, noticeable shifts are observed at 29.7°, 44.1°, and 63.4°. Overall, the XRD analysis of the sample reveals well-defined peaks corresponding to the iron selenide, nickel selenide, and cobalt selenide phases. These results offer valuable insights into the composition and crystalline structure of the material under investigation, contributing to a comprehensive characterization.

In an alternative approach, the estimation of pore size and distribution for the NiCoFeSe was carried out using adsorption–desorption isotherms and Brunauer–Emmett–Teller (BET) characterization. The nitrogen adsorption–desorption isotherm of the NiCoFeSe exhibits a

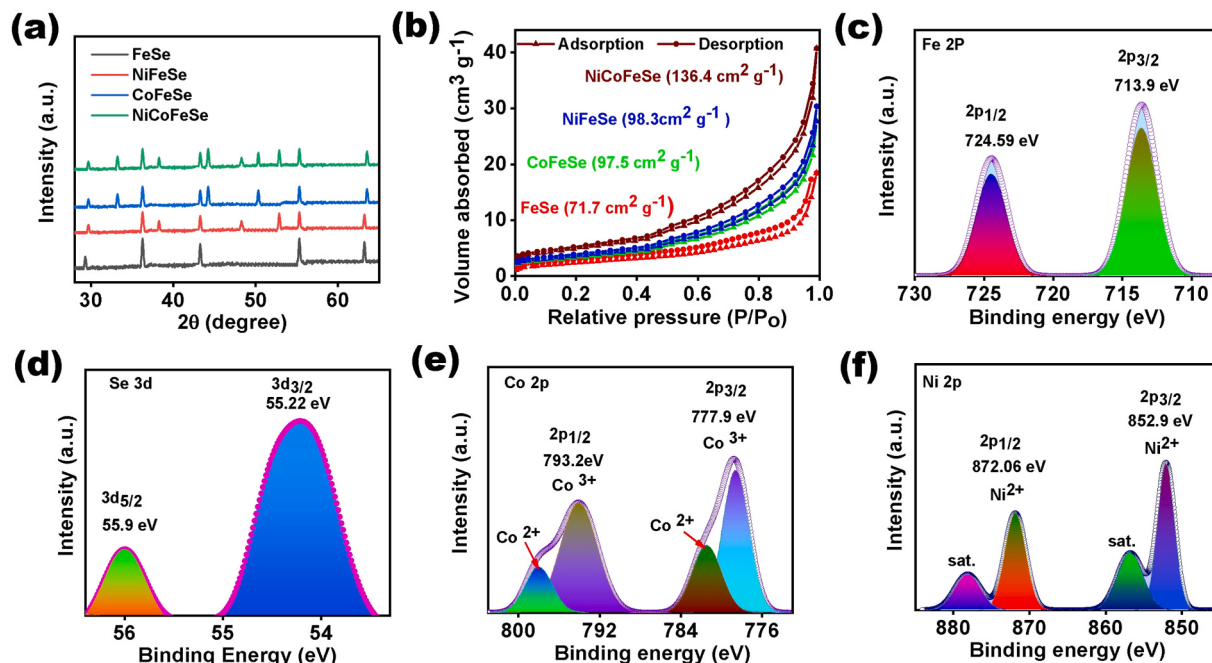


Fig. 2. (a) XRD Analysis of FeSe, NiFeSe, CoFeSe and NiCoFeSe, (b) BET Analysis of FeSe, NiFeSe, CoFeSe and NiCoFeSe, (c) XPS Analysis of Fe in NiCoFeSe, (d) XPS Analysis of Se in NiCoFeSe, (e) XPS Analysis of Co in NiCoFeSe, (f) XPS Analysis of Ni in NiCoFeSe.

distinct type-IV hysteresis loop, confirming the presence of a mesoporous structure, as illustrated in **Fig. 2b**. Based on BET surface area calculations, the surface areas are determined to be 71.7, 97.5, 98.3 and 136.4 cm² g⁻¹ for FeSe, CoFeSe, NiFeSe and NiCoFeSe, respectively. Furthermore, the pore-size analysis reveals the mesoporous characteristics of the NiCoFeSe, as depicted in **Fig. S1b**. The increased surface area and mesoporous attributes of the NiCoFeSe enhance its catalytic performance in both the OER and HER. Consequently, this leads to the generation of more electrocatalytically active sites and efficient charge transfer pathways.

Furthermore, X-ray photoelectron spectroscopy (XPS) analysis was conducted to investigate the elemental composition of the material. The full spectrum XPS results, as shown in **Fig. S2b**, confirm the presence of all elements. Upon analyzing the individual XPS spectra for each element, the following observations came to light. In **Fig. 2c**, the XPS spectrum of Fe exhibits peaks at 714.7 and 724.59 eV, corresponding to the 2p_{3/2} and 2p_{1/2} energy levels, respectively. Notably, these peaks display shift towards higher binding energies when compared to those of FeSe (refer to **Fig. S20**) [58]. These peaks signify the distinctive electronic transitions of Fe within the NiCoFeSe. The XPS analysis of Se, as depicted in **Fig. 2d**, reveals peaks at 55.9 and 55.22 eV, corresponding to the 3d_{5/2} and 3d_{3/2} energy levels, respectively. These peaks exhibit a distinct shift to lower binding energies in contrast to those of FeSe (refer to **Fig. S20**) [59]. The observation of opposite shifts in the Fe 2p and Se 3d peaks suggests a partial electron transfer within NiCoFeSe. **Fig. 2e** illustrates the XPS spectrum for Co, unveiling two distinct peaks at 777.9 and 793.2 eV, corresponding to the 2p_{3/2} and 2p_{1/2} energy levels, respectively [60]. These peaks offer valuable insights into the electronic configuration and chemical state of Co within the NiCoFeSe. Furthermore, in the high-resolution XPS spectrum of Ni 2p (depicted in **Fig. 2f**), two distinctive peaks emerge at 852.9 and 872.06 eV, corresponding to the Ni 2p_{3/2} and Ni 2p_{1/2} states of Ni, respectively [61]. Additionally, two satellite peaks are discernible at 857.66 eV and 879.01 eV. Overall, the XPS analysis provides valuable insights into the elemental composition and chemical states of Ni, Co, Fe, and Se within the material, contributing to a comprehensive understanding of its properties. Further, the results of the ICP-MS test confirm the presence of Ni, Co, Fe, and Se, as detailed in **Table S5**.

3.2. Evaluating catalyst performance

3.2.1. OER and UOR activity

In our research, we conducted a study on the OER activity of different catalysts. The catalysts we examined included NF, FeSe, CoFeSe, NiFeSe, RuO₂, and NiCoFeSe. To carry out our experiments, we employed a standard setup with three electrodes in a 1 M KOH electrolyte solution. In order to assess the OER activity of these catalysts, we obtained data through Linear Sweep Voltammetry (LSV) for NF, FeSe, CoFeSe, NiFeSe, RuO₂, and NiCoFeSe. The resulting LSV curves were plotted in the **Fig. 3a**. Through the analysis of the LSV data presented in **Fig. 3a**, we performed calculations to determine the overpotential values for FeSe, CoFeSe, NiFeSe, RuO₂, and NiCoFeSe catalysts. These overpotential values were then visualized in **Fig. 3b**. Specifically, when aiming for current densities of 50 and 100 mAcm⁻², the corresponding overpotential values were obtained as follows: FeSe (380, 430 mV), CoFeSe (340, 410 mV), NiFeSe (330, 390 mV), and NiCoFeSe (230, 330 mV). It is noteworthy that NiCoFeSe exhibited the lowest overpotential compared to counter catalysts. These findings suggest that NiCoFeSe is a highly promising candidate for industrial water splitting applications due to its lower overpotential, particularly at higher current densities. The overpotential values provide valuable insights into the catalytic efficiency of the various catalysts for the OER. Moreover, NiCoFeSe shows excellent OER activity compare to recent reported catalyst as given in **Table S2**. In addition to investigating the OER activity of FeSe, CoFeSe, NiFeSe, RuO₂, and NiCoFeSe catalysts, we also evaluated their performance using the Tafel method. The results of this

analysis are presented in the **Fig. 3c**. Through the examination of the Tafel analysis, it was noted that NiCoFeSe displayed the smallest Tafel slope (38.4 mV dec⁻¹) in comparison to counter catalysts. This observation signifies that the NiCoFeSe catalyst exhibits enhanced reaction kinetics for the OER when compared to FeSe, CoFeSe, NiFeSe, and RuO₂. A lower Tafel slope indicates a more efficient and rapid performance in the OER, thereby highlighting the superior reaction kinetics of the NiCoFeSe catalyst.

we quantitatively determined the active sites by calculating the atomic concentration of the Faraday moiety on the catalyst surface. The atomic concentration of the Faraday moiety for NiCoFeSe was found to be 3.25×10^{18} atoms cm⁻², whereas the counter catalysts have a lower concentration as displayed in **Fig. S3**. This result serves as strong evidence supporting the presence of a sufficient number of active sites in NiCoFeSe. Having a higher atomic concentration of the Faraday moiety on the catalyst surface implies that there are more sites available for electrocatalytic reactions. These active sites provide reaction sites for the reactants and facilitate the electron transfer process, leading to improved catalytic performance. The presence of sufficient active sites is crucial for achieving high catalytic activity, selectivity, and overall electrochemical performance. An alternative approach for evaluating catalytic performance is through electrochemical surface area (ECSA) analysis. ECSA values were determined by examining the non-faradaic double-layer region of the cyclic voltammetry (CV) curve. The results presented in **Fig. 3d** and **Fig. S4** reveal a significantly highest ECSA value for NiCoFeSe compared to FeSe, CoFeSe, and NiFeSe. This finding provides compelling evidence that NiCoFeSe possesses a larger electrochemically active surface area, indicating its potential as a highly effective catalyst. The increased ECSA value suggests the presence of a greater number of active sites in NiCoFeSe, which can greatly enhance its catalytic performance across electrochemical water splitting. These findings highlight the favorable characteristics of NiCoFeSe and its suitability for improving electrochemical activity in water splitting. Furthermore, the innate reactivity of the active sites found on electrocatalysts operating under standard reaction conditions can be quantified using their Turnover Frequency (TOF) and TOF is calculated using S12 equation. At an overpotential of 300 mV, NiCoFeSe exhibits a TOF value of 1.25 S⁻¹, surpassing the TOF values of FeSe, CoFeSe, and NiFeSe, as illustrated in **Fig. S23**. This suggests that NiCoFeSe is a highly promising candidate for enhancing electrochemical water splitting. Additionally, when compared to recent reports, NiCoFeSe demonstrates good performance, as shown in **Table S5**.

Moreover, the stability of NiCoFeSe as an OER catalyst was evaluated through chronopotentiometry measurements. The results demonstrate that NiCoFeSe exhibits excellent stability even at high current densities, as depicted in **Fig. 3h**. The catalyst maintains its performance over a period of 200 h without significant degradation. Furthermore, the durability of NiCoFeSe was confirmed by examining the LSV curve after the stability test, as shown in **Fig. 3i**. The LSV curve indicates that NiCoFeSe retains its excellent catalytic activity and durability, further reinforcing its potential as a reliable and long-lasting OER catalyst. These findings underscore the stability and durability of NiCoFeSe, positioning it as a promising candidate for practical applications in the field of electrocatalysis. To delve deeper into the stability assessment of NiCoFeSe, we conducted a comprehensive morphological analysis employing SEM and TEM. As evident in **Fig. S5a-b** and **Fig. S6a-b**, the outcome of both SEM and TEM analyses indicated that the morphology of NiCoFeSe is similar even after subjecting it to stability testing. This compelling observation suggests that NiCoFeSe maintains its structural integrity, showing no significant morphological changes during the stability assessment. Furthermore, the stability of NiCoFeSe is corroborated by the XPS results, as depicted in **Fig. S21**, and the XRD findings, as illustrated in **Fig. S22**.

The electrochemical performance of NiCoFeSe nanospheres was examined in the context of the UOR using a three-electrode system with 1.0 M KOH and 0.33 M urea electrolytes. **Fig. 3j** displays the results of

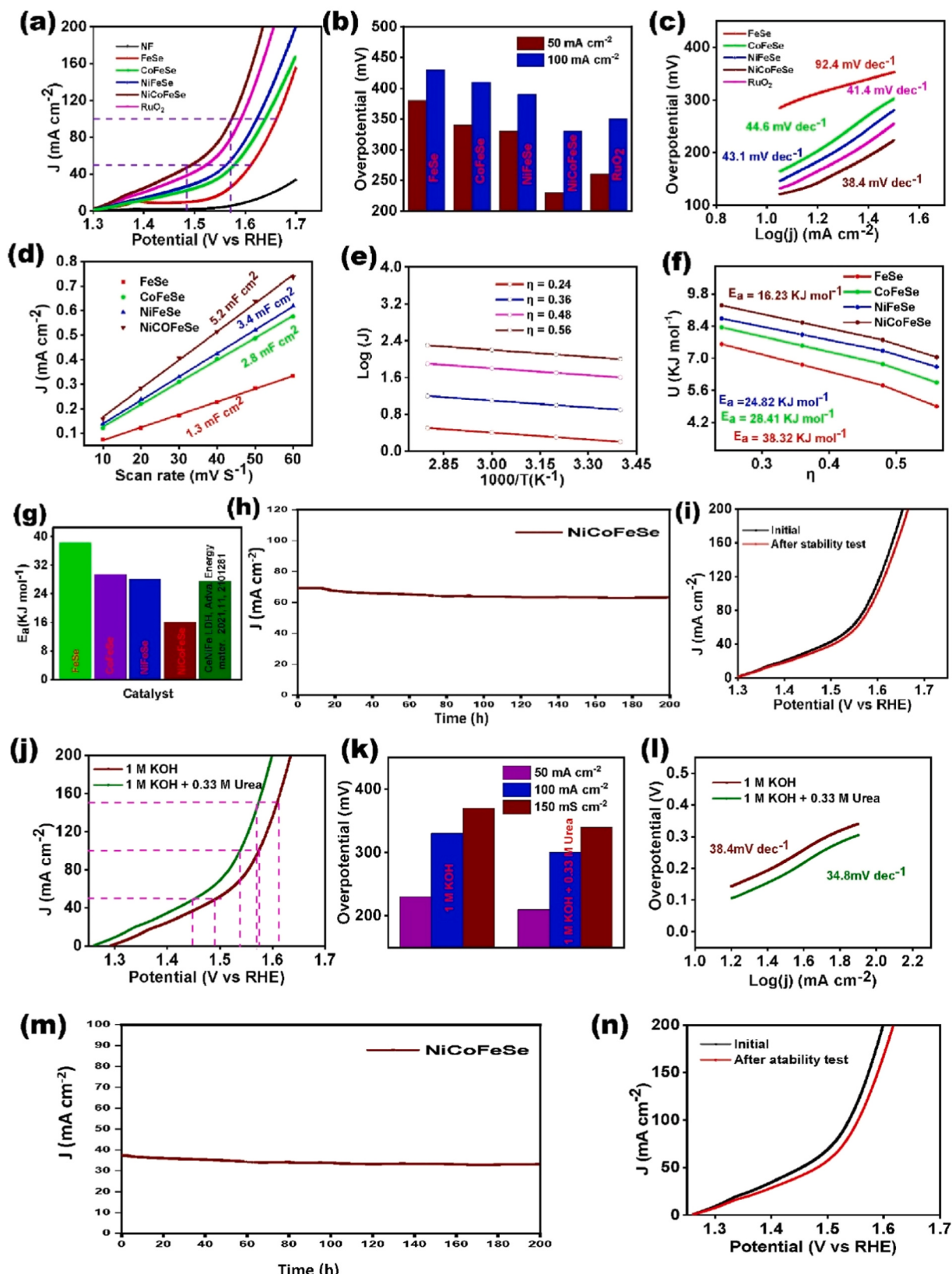


Fig. 3. (a) Electrochemical LSV Plot for OER, (b) Overpotential Analysis for OER, (c) Tafel Slope Determination for OER, (d) Variations in Scan Rate for ECSA Measurement, (e) Arrhenius Plot at Different Voltage Levels, (f) Results of Activation Energy Calculation, (g) Comparison of Activation Energies, (h) Stability Testing of NiCoFeSe for OER, (i) Post-Stability LSV of NiCoFeSe for OER, (j) LSV Comparison of NiCoFeSe for UOR and OER, (k) Overpotential Comparison for UOR and OER, (m) Chronoamperometry Testing for UOR, (n) Post-Stability LSV of NiCoFeSe for UOR.

LSV polarization curves for the NiCoFeSe, both with and without the urea electrolyte. It is worth noting that the NiCoFeSe exhibited remarkable activity for the UOR when the urea electrolyte was present, as indicated by the significantly lower overpotentials (as depicted in Fig. 3k) required to achieve current densities of 50, 100 and 150 mA cm^{-2} : 210, 300, and 340 mV, respectively. These values are notably lower than those observed in the alkaline electrolyte, where overpotentials of 230, 330, and 370 mV were necessary. This suggests that the NiCoFeSe performs exceptionally well in the presence of the urea electrolyte, indicating enhanced performance compared to the alkaline electrolyte conditions. Furthermore, a deeper analysis reveals that the Tafel slope of NiCoFeSe in the urea electrolyte is smaller, measuring at 34.8 mV dec^{-1} , in contrast to the steeper slope of 38.4 mV dec^{-1} observed in the alkaline electrolyte. This difference in Tafel slopes signifies enhanced UOR kinetics, as effectively demonstrated in Fig. 3l. The catalytic stability of NiCoFeSe underwent rigorous scrutiny through a continuous 200 h exposure to a constant voltage. The findings, as visually represented in Fig. 3m, unequivocally establish that NiCoFeSe demonstrates remarkable stability throughout the entire testing period. Moreover, the overpotential exhibited by NiCoFeSe remained virtually unaltered both before and after the durability test, as clearly indicated in Fig. 3n.

3.2.2. Analysis of kinetic energy

The investigation into the kinetic energy barrier associated with the

OER involved a detailed analysis of activation energy (E_a) through the examination of LSV curves conducted at various temperatures (refer to Fig. S7). It is worth noting that E_a is intricately connected to the electronic configuration and composition of the electrocatalyst materials employed in the study. To determine E_a values accurately, Arrhenius plots were constructed, where the natural logarithm of the OER current was plotted against the reciprocal of the absolute temperature ($\frac{\partial(\log i)}{\partial(1/T)} = -\frac{E_a}{2.303R}$) as illustrated in Fig. 3e. The exploration of E_a in the context of OER kinetics is a critical aspect of understanding the reaction's thermodynamics and kinetics. The analysis of LSV curves at different temperatures provides insights into how the activation energy varies under different conditions, shedding light on the electrocatalyst's performance. Additionally, the construction of Arrhenius plots aids in discerning the temperature-dependent behavior of the OER, offering valuable information for the design and optimization of electrocatalytic materials for this important reaction. The mathematical representation of the OER current can be formulated as $i_k = B \exp(-U/RT)$, where U represents the overall activation energy, and B stands for the pre-exponential factor. The determination of E_a for the OER was ultimately achieved using the formula $U = E_a - \alpha\eta$, where α is an experimental constant (as depicted in Fig. 3f) [62,63]. As illustrated in Fig. 3g, the calculated E_a value for NiCoFeSe was found to be 16.23 kJ mol^{-1} , significantly lower when compared to FeSe (38.32 kJ mol^{-1}), CoFeSe (29.5 kJ mol^{-1}), NiFeSe (28.0 kJ mol^{-1}), and CeNiFe-LDH

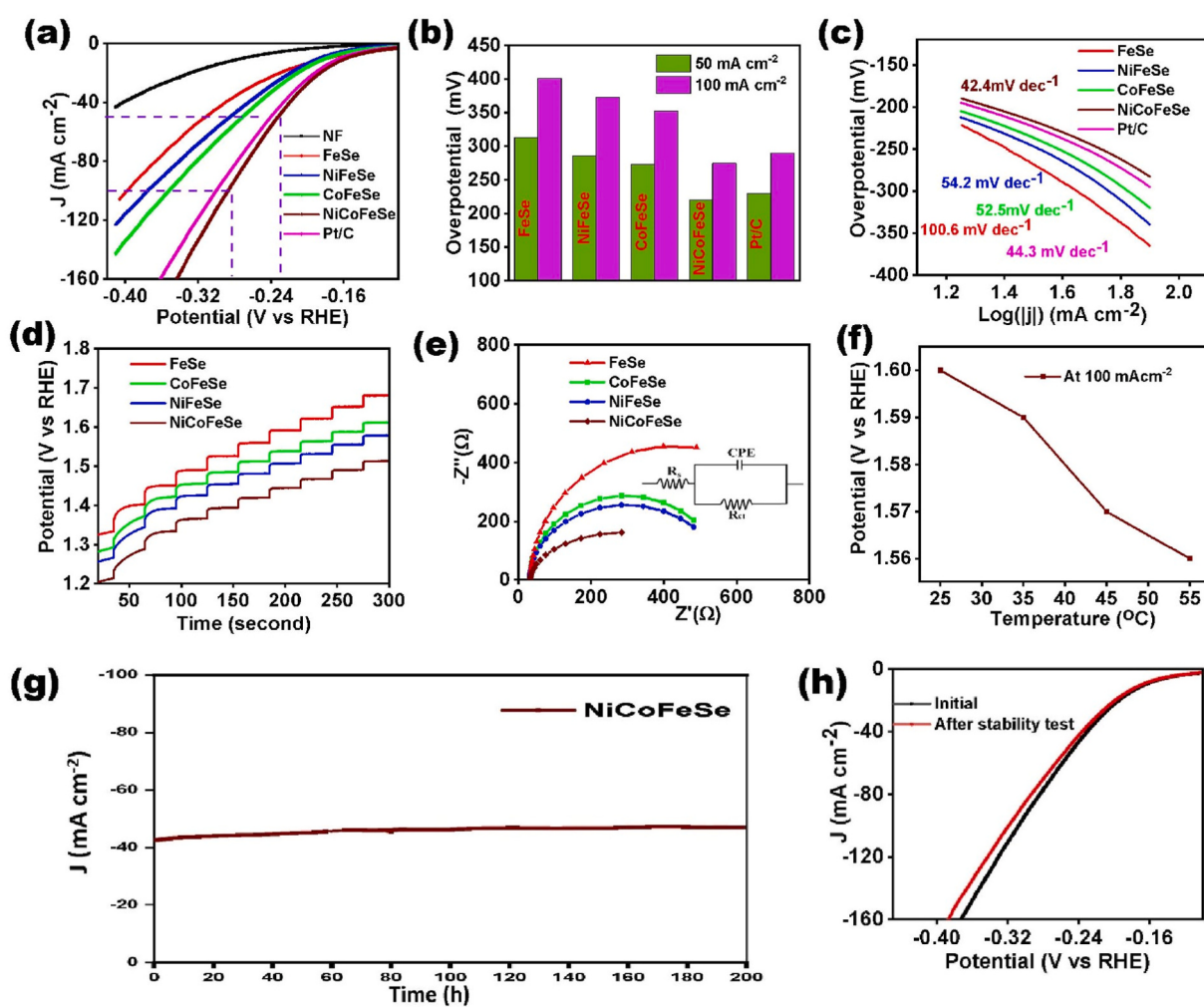


Fig. 4. (a) Displays the LSV plot, (b) Focuses on the overpotential data, (c) Examines the Tafel slope, (d) Demonstrates the voltage requirements across a range of low to high current density, (e) Presents the results from the EIS test, (f) Illustrates the voltage required at various temperatures while maintaining a current of 100 mA cm^{-2} , (g) Shows the chronoamperometry results, (h) Provides LSV data after conducting stability tests.

(27.6 kJ mol⁻¹) [62]. These findings underscore that NiCoFeSe exhibits a reduced kinetic barrier in the context of the OER. This lowered activation energy suggests that NiCoFeSe may serve as a more efficient electrocatalyst for facilitating the OER, potentially making it a promising candidate for water splitting.

3.2.3. HER activity

In our research, we explored the HER activity of various catalysts, namely NF, FeSe, CoFeSe, NiFeSe, Pt/C, and NiCoFeSe. We conducted these experiments using a standard three-electrode setup immersed in a 1 M KOH electrolyte solution. To assess the HER activity of these catalysts, we collected LSV data for NF, FeSe, CoFeSe, NiFeSe, Pt/C, and NiCoFeSe, and these LSV curves are illustrated in Fig. 4a. By closely analyzing the LSV data presented in Fig. 4a, we were able to compute and determine the overpotential values for FeSe, CoFeSe, NiFeSe, NiCoFeSe, and Pt/C. These calculated overpotential values were subsequently visualized in Fig. 4b. To achieve current densities of 50 and 100 mA cm⁻², the determined overpotential values were as follows: FeSe (313, 401 mV), CoFeSe (286, 373 mV), NiFeSe (273, 352 mV), Pt/C (230, 390 mV), and NiCoFeSe (220, 275 mV). Notably, NiCoFeSe exhibited the most favorable overpotential, surpassing FeSe, CoFeSe, NiFeSe, and Pt/C. In light of these results, NiCoFeSe stands out as a promising candidate for industrial applications involving water splitting, especially at higher current densities. These overpotential values offer valuable insights into the catalytic efficiency of the various catalysts for the HER. Furthermore, NiCoFeSe displays outstanding HER activity when compared to recently reported catalysts, as presented in Table S3. In addition to investigating the HER activity of FeSe, CoFeSe, NiFeSe, NiCoFeSe, and Pt/C catalysts, we also evaluated their performance using the Tafel method, and the outcomes are depicted in Fig. 4c. The Tafel analysis revealed that NiCoFeSe displayed the most favorable Tafel slope (42.4 mV dec⁻¹) compared to FeSe (100.6 mV dec⁻¹), CoFeSe (52.5 mV dec⁻¹), NiFeSe (54.2 mV dec⁻¹), and Pt/C (44.3 mV dec⁻¹). This indicates that the NiCoFeSe catalyst exhibits superior reaction kinetics for the HER when compared to FeSe, CoFeSe, and NiFeSe. A lower Tafel slope signifies a more efficient and rapid HER performance, underscoring the exceptional reaction kinetics of the NiCoFeSe catalyst. Furthermore, we conducted measurements to determine the voltage required to increase the current density from low to high value, as shown in Fig. 4d. The results clearly indicate that the NiCoFeSe exhibited a lower voltage requirement to achieve the desired current density. Our study also explored the charge transfer behavior at the interface between the electrolyte and catalyst. As depicted in Fig. 4e and Table S1, the Nyquist plots clearly demonstrate that NiCoFeSe exhibits significantly lower charge transfer resistance compared to FeSe, CoFeSe, and NiFeSe, suggesting a notable enhancement in electron mobility and faster electron movement. Furthermore, our investigation delved into the impact of temperature on the required voltage, leading to a noteworthy observation. As depicted in Fig. 4f and Fig. S7, there is a distinct trend: an increase in temperature corresponds to a decrease in the required voltage. This significant discovery not only sheds light on the behavior of the system but also underscores the potential viability of NiCoFeSe as an exceptionally robust candidate for industrial applications.

Moreover, the durability of the NiCoFeSe was assessed through chronoamperometry (i-t) measurements over a period of 200 h. The results indicated that there was minimal decrease in current density after continuous operation, highlighting the outstanding stability of the NiCoFeSe in HER, as visually presented in Fig. 4g. Furthermore, the long-term performance of the NiCoFeSe was evaluated by examining the degradation in the LSV curve after 200 h. Fig. 4h illustrates that the NiCoFeSe exhibited only minor degradation, further confirming its durability and sustained efficiency. Furthermore, to enhance our understanding of the catalyst's morphological and structural attributes under continuous operation, we conducted additional analyses. SEM was employed, and the results, presented in Fig. S8a-b at various

magnifications, exhibited a morphology highly reminiscent of the original NiCoFeSe. Moreover, elemental mapping, as depicted in Fig. S8c, conclusively confirmed the presence of all constituent elements. Moreover, Field Emission Transmission Electron Microscopy (FE-TEM) yielded results that underscored the remarkable stability of NiCoFeSe's morphology even after enduring the rigorous stability tests. These findings, showcased in Fig. S9, provide compelling evidence of the material's structural robustness, further bolstering its potential for enduring and effectively contributing to various applications. Additionally, the stability of NiCoFeSe is supported by the XPS outcomes, as shown in Fig. S21, and the XRD results, as displayed in Fig. S22.

3.3. Alkaline water electrolyzer

3.3.1. Two electrode electrolyzer

Based on the remarkable performance in both the HER and OER, NiCoFeSe emerges as a highly promising candidate for overall water splitting applications using a two-electrode electrolyzer setup. The two-electrode LSV analysis, as presented in Fig. 5a, clearly illustrates the voltage required to achieve a current density of 10 mA cm⁻² for FeSe (-) || FeSe (+), CoFeSe (-) || CoFeSe (+), NiFeSe (-) || NiFeSe (+), NiCoFeSe (-) || NiCoFeSe (+), and RuO₂ (-) || Pt/C (+) setups, which are 1.58 V, 1.55 V, 1.54 V, 1.51 V and 1.52 V respectively. Its even lower voltage requirements compared to the conventional RuO₂ || Pt/C reference electrode position NiCoFeSe as an attractive option for driving water splitting reactions. Stability is a crucial characteristic for a catalyst to be considered a good candidate for electrochemical water splitting. In order to evaluate the stability of NiCoFeSe, we conducted chronoamperometry tests. The analysis results, presented in Fig. 5b, reveal that NiCoFeSe (-) || NiCoFeSe (+) exhibits excellent stability even at higher current densities. The current density shows low decay over the duration of the test, indicating the catalyst's ability to maintain its electrochemical performance without significant degradation. Furthermore, to assess the durability of NiCoFeSe (-) || NiCoFeSe (+), we examined the LSV curve after the stability test. As shown in Fig. 5c, the LSV curve demonstrates that there is no noticeable degradation in the catalytic activity of NiCoFeSe (-) || NiCoFeSe (+). This suggests that NiCoFeSe maintains its performance and stability even after the stability test, indicating its robustness and suitability for long-term applications. The exceptional stability observed in both the chronoamperometry test and the LSV analysis highlights the reliability and durability of NiCoFeSe (-) || NiCoFeSe (+) as an electrochemical water splitting catalyst. These findings are essential for advancing the development of efficient and sustainable water splitting technologies for hydrogen production. Furthermore, the half-cell voltage, calculated by considering the difference between the anode and cathode voltages as depicted in Fig. 5d. These findings highlight the significant potential of NiCoFeSe as a highly efficient catalyst for overall water splitting. The lower voltage requirements of NiCoFeSe indicate its ability to contribute to the development of more energy-efficient and cost-effective systems for clean hydrogen production through water splitting. This further supports its potential for renewable energy applications and the transition towards sustainable energy sources.

In order to elucidate the water splitting mechanism and the direction of electron movement facilitated by NiCoFeSe, we provide a detailed illustration in Fig. 5e. This mechanism sheds light on the catalytic process and highlights the role of NiCoFeSe in driving the electrochemical reactions involved in water splitting. Fig. 5f presents a digital image showcasing the setup of a conventional two-electrode electrolyzer paired with a single-cell battery. To thoroughly evaluate the performance of this configuration, we conducted an extensive analysis, as elaborated in Video S1. The results reveal that the two-electrode electrolyzer operates efficiently when powered by a single battery cell. This observation underscores the reliability of the system when utilizing a solitary battery source. Moreover, to assess the performance of NiCoFeSe in comparison to previously reported results, a comparative

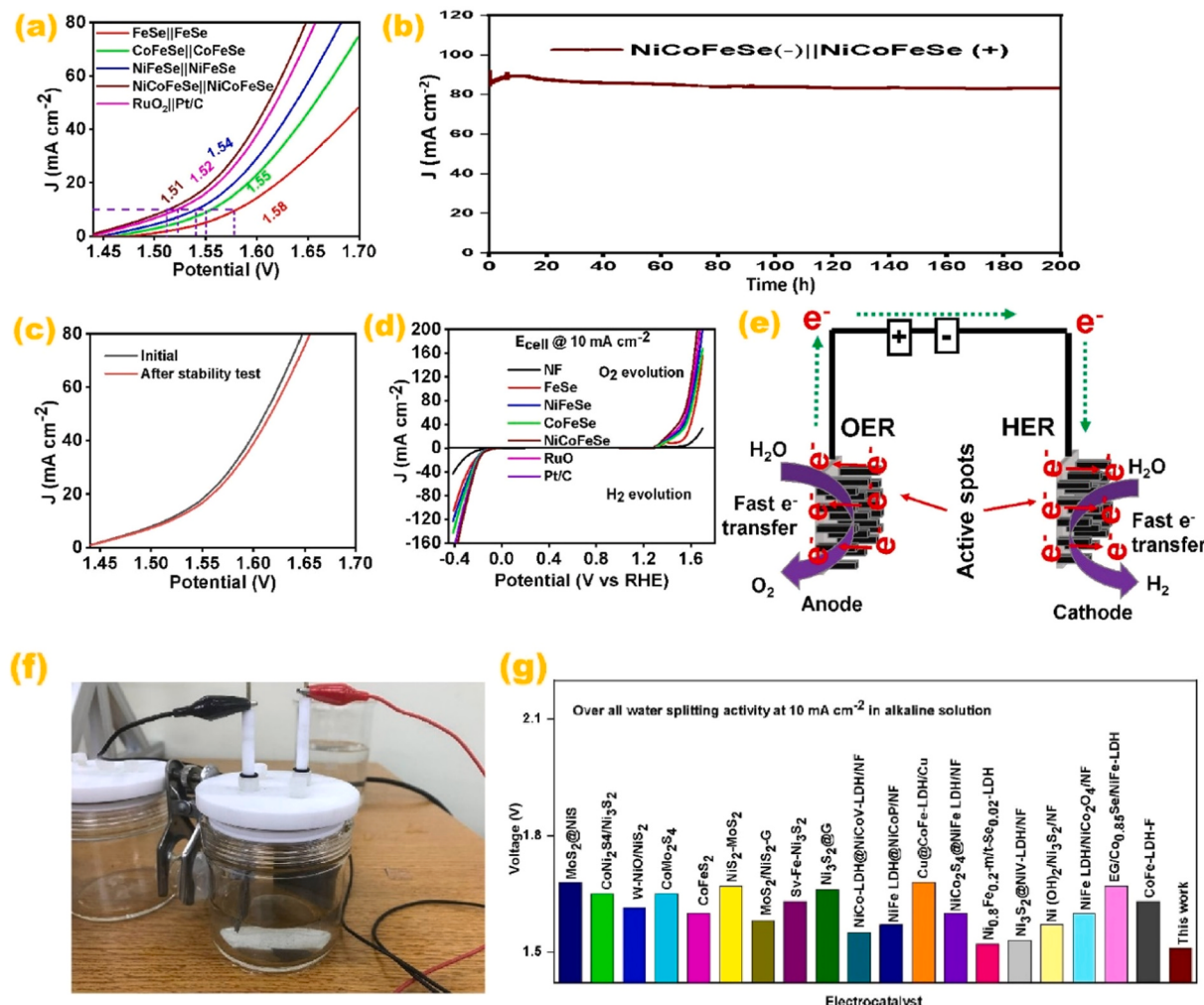


Fig. 5. (a) Demonstrates LSV results for the two-electrode setup of catalysts. (b) Illustrates chronoamperometry data at 1.68 V, (c) Displays LSV results after a stable test (d) Represents half-cell voltage data, (e) Provides a schematic diagram, (f) Depicts a two-electrode electrolyzer coupled with a battery cell, (g) Compares our findings with previously reported records.

analysis is presented in Fig. 5g. This allows us to gauge the effectiveness of NiCoFeSe as a water splitting catalyst and to evaluate its performance against established benchmarks. These experimental measurements, along with the proposed mechanism and comparative analysis, provide comprehensive insights into the water splitting capabilities of NiCoFeSe. The observed gas production, the understanding of the catalytic mechanism, and the performance comparison contribute to our understanding of NiCoFeSe as a highly promising candidate for efficient and sustainable water splitting applications.

Supplementary material related to this article can be found online at doi:10.1016/j.apcatb.2023.123635.

3.3.2. PV-EC alkaline water electrolyzer

In our research, we conducted a series of experiments and tests focused on the direct assembly of solar cells (photovoltaic or PV) as a charge source with NiCoFeSe serving as both the anode and cathode. We illustrated these setups using three-dimensional models, as shown in Fig. 6a for the rigid device and Fig. 6b for the flexible device. These models showcase the innovative configuration in which NiCoFeSe functions as both the anode and cathode, seamlessly connected to the solar cell without the need for traditional wiring. This novel approach introduces a unique mechanism for photovoltaic-electrochemical applications, particularly in the context of overall water splitting. By eliminating the requirement for extensive wiring, our system simplifies

the setup and mitigates power losses due to extended wire resistance. Consequently, this design enhancement leads to an improved system efficiency and a substantial reduction in overall complexity. To provide a visual representation of our work, we have included digital photographs of both the rigid device (Fig. 6c) and the flexible device (Fig. 6d). Additionally, for those interested in the fabrication process of both the rigid and flexible devices, we have provided detailed information in Fig. S11 - S14.

The performance of the photovoltaic (PV) component in this configuration is effectively illustrated through the I-V (current-voltage) curve analysis. Our observations reveal noteworthy characteristics of the PV system's behavior. Firstly, in the absence of illumination (in the dark), we measure an open-circuit voltage of 1.75 V, as clearly depicted in Fig. 6c. This voltage level serves as a baseline reference for the system's behavior without any external light source. However, when the PV component is exposed to one sun's worth of illumination, as shown in Fig. 6e, there is a significant increase in the open-circuit voltage, reaching a level of 2.0 V. This indicates that the PV system efficiently harnesses and utilizes the solar energy from this light source. These observations underscore the PV component's ability to generate a substantial voltage differential when exposed to sunlight, demonstrating its effectiveness in converting solar energy into usable electrical power. In addition, the Solar-to-Hydrogen (STH) efficiency is estimated using, $STH(\%) = \frac{j \times 1.23 \times F_E}{I_0} \times 100$, j is current density of device, F_E is

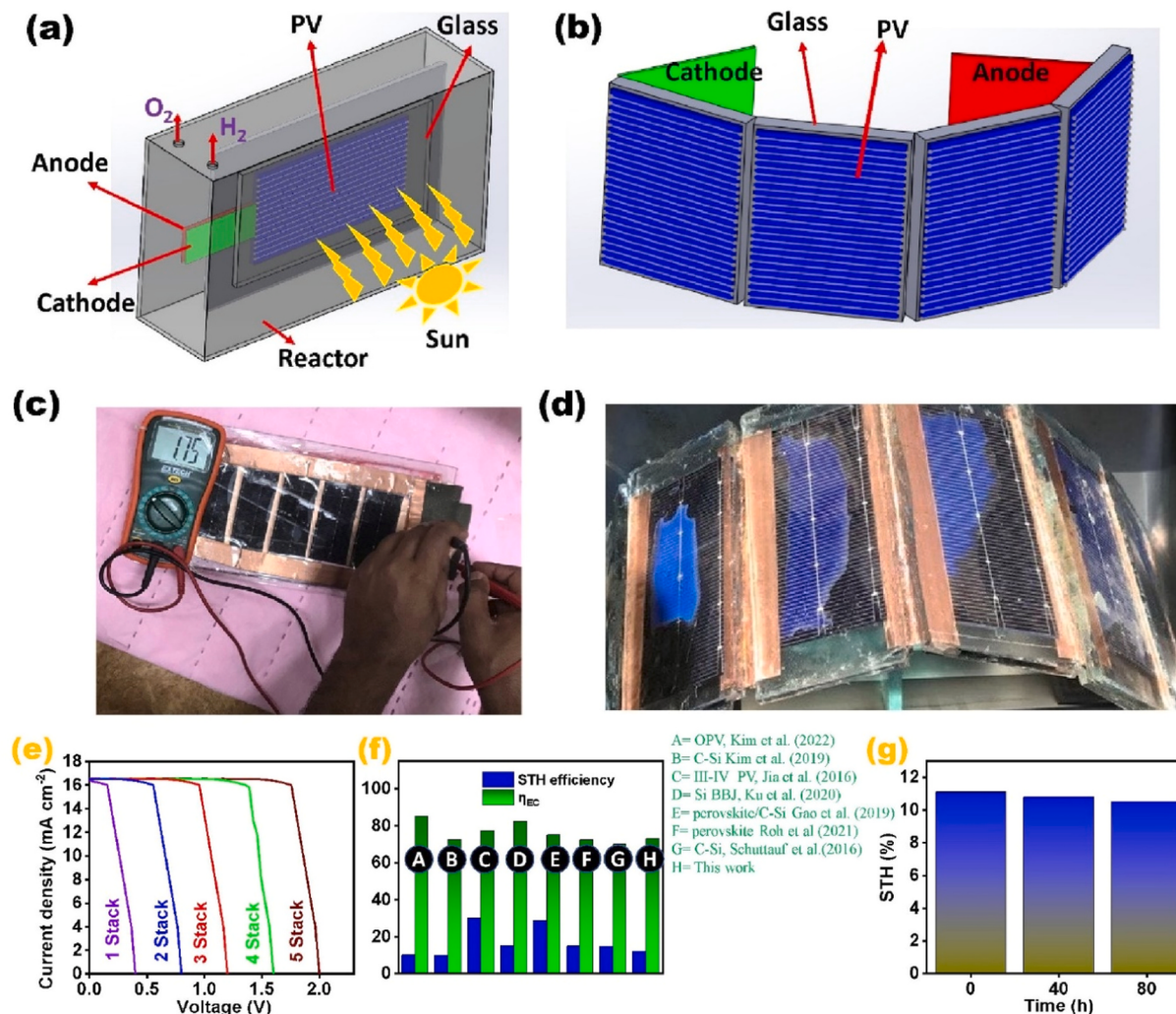


Fig. 6. Presents various aspects of our study's photovoltaic-electrochemical (PV-EC) system (a) Depicts a model of the rigid PV-EC device, (b) Illustrates a model of the flexible PV-EC device, (c) Displays a digital photograph of the fabricated rigid PV-EC device, (d) Shows a digital photograph of the fabricated flexible PV-EC device, (e) Demonstrates the I-V curve of the photovoltaic (PV) component, (f) Compares the Solar-to-Hydrogen (STH) and electrochemical (EC) efficiency of the PV-EC system with previous reports, (g) Evaluates the stability of the PV-EC device over time.

Faradaic efficiency, I_o is incident light power (100 mW cm^{-2} , as given in Fig. S13). In our study, our device achieved an impressive STH efficiency of 11.1%. This result was accompanied by a remarkable EC conversion efficiency of 73.3%. Together, these numbers signify a significant achievement in our research, where approximately 15.14% of the PV energy input was successfully transformed into H_2 production and good candidate compare to recent reports, as clearly demonstrated in Fig. 6f. This outcome underscores the potential of our device for efficient and sustainable energy conversion, holding promise for various practical applications. Additionally, we conducted a stability assessment of the device over an extended 80 h duration, as presented in Fig. 6g. The results reveal a minimal decay in the device's performance, indicating its robust and reliable operation over an extended period. This finding is particularly promising for practical applications where long-term stability is crucial, underscoring the device's potential for sustained and dependable performance. To conclude, we conducted real electrolyzer demonstrations with both the rigid PV-EC device (Video S2) and the flexible PV-EC device (Video S3). These demonstrations vividly showcase the formation of oxygen at the anode and hydrogen at the cathode, affirming the practical functionality of our systems in splitting water into its constituent gases. These real-world demonstrations validate the feasibility and efficiency of our PV-EC setups for clean and sustainable hydrogen production, emphasizing their potential significance in

renewable energy applications. Therefore, the wireless assembly of PV and NiCoFeSe represents a promising approach for integrating photovoltaics with electrochemical water splitting. This configuration eliminates the need for wiring, simplifies the system, reduces power losses, and enhances overall efficiency. These findings highlight the potential of this approach for advancing photovoltaic-electrochemical applications for water splitting.

Supplementary material related to this article can be found online at doi:10.1016/j.apcatb.2023.123635.

Supplementary material related to this article can be found online at doi:10.1016/j.apcatb.2023.123635.

3.3.3. Commercial zero-gap alkaline water electrolyzer

In Fig. 7a, the model presents an economically efficient method for hydrogen production through an Anion Exchange Membrane Water Electrolyzer (AEMWE) that does not rely on precious metals. This development involves the creation of a membrane electrode assembly (MEA) by combining NiCoFeSe as both the OER and HER electrocatalyst with an anion exchange membrane (Sustainion™ X37–50 RT). This membrane serves as an ionic separator in a 1 M KOH solution. Fig. 7b illustrates the LSV curves of the AEMWE using NiCoFeSe as the anode and cathode materials. The AEMWE operates with 1 M KOH as the circulating medium at a temperature of 50 °C (the detail is given in

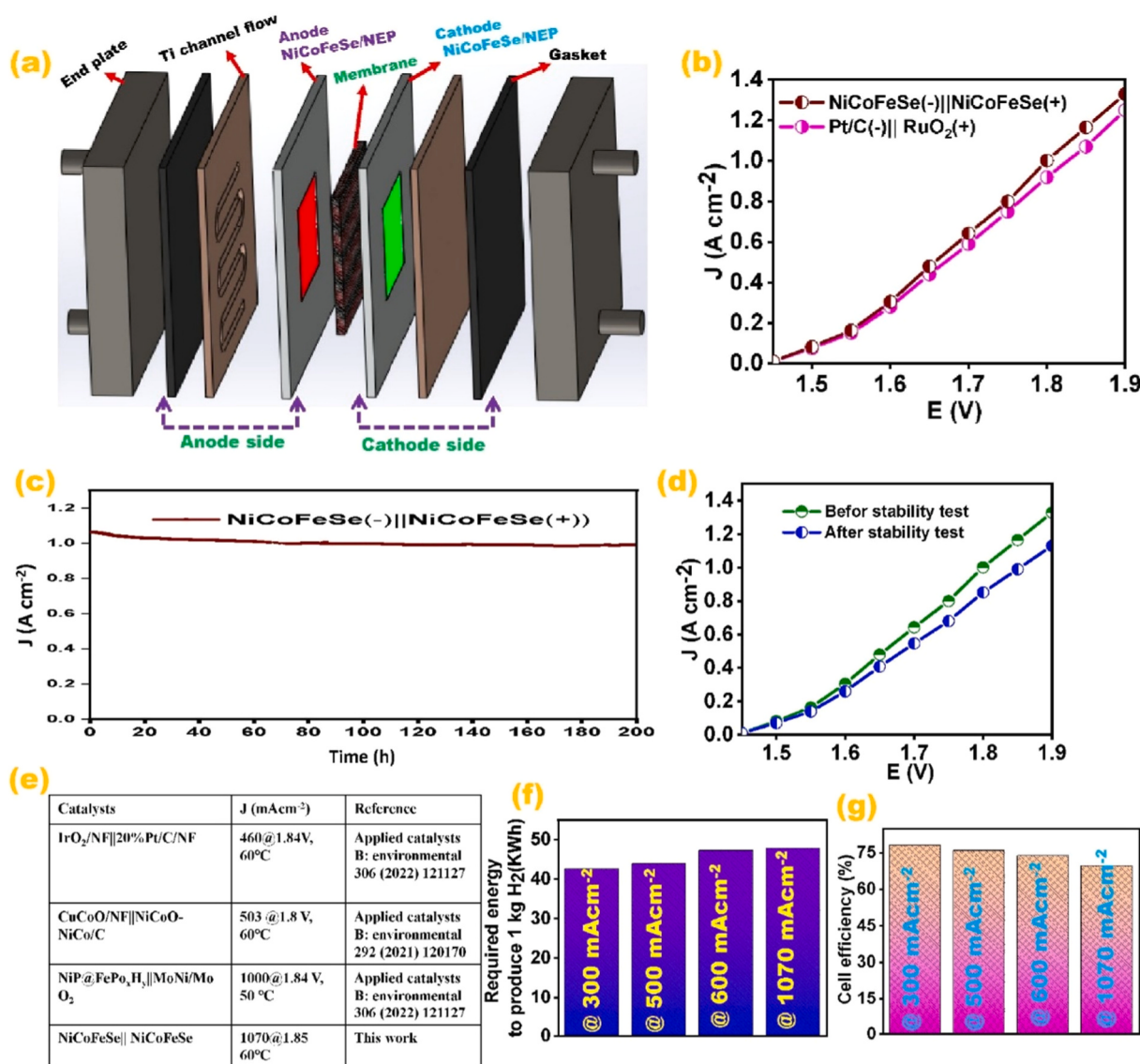


Fig. 7. Visualizing Different Aspects of the Zero Gap Alkaline Electrolyzer, (a) Model Representation of the Zero Gap Alkaline Electrolyzer, (b) LSV Performance of the Zero Gap Electrolyzer, (c) Stability Assessment of the Electrolyzer, (d) LSV Results Post Stability Test, (e) Comparative Analysis with Recent Research Findings, (f) Energy Consumption for 1 kg H₂ Production at Varying Current Densities, (g) Cell Efficiency at various Current Densities.

Video S4). Notably, the AEMWE exhibits exceptional performance, producing an activity of 1.07 A cm⁻² at 1.85 V, surpassing the performance of conventional alkaline water splitting electrolyzers. This development holds significant promise for the field of hydrogen production, as it offers an economically efficient and sustainable alternative to precious metal-dependent processes, potentially driving advancements in clean energy technologies.

Supplementary material related to this article can be found online at doi:10.1016/j.apcatb.2023.123635.

The durability assessment of the MEA within the AEMWE was conducted at an operating voltage of 1.85 V. An impressive finding emerged, particularly concerning the exceptional stability demonstrated by the NiCoFeSe/NFP(+)||NiCoFeSe/NFP(-) configuration. This stability remained largely intact over a prolonged period of 200 h, as depicted in Fig. 7c. Furthermore, the post-stability test LSV results, shown in Fig. 7d, provide additional evidence of the remarkable stability exhibited by NiCoFeSe/NFP(+)||NiCoFeSe/NFP(-). To gauge the efficacy of hydrogen generation, gas chromatography (GC) was employed as the measuring tool. The results revealed a hydrogen generation rate of 22.4 mL per minute with an impressive purity level of 99.995%. This

purity level closely approaches the standards of commercially available hydrogen, which typically boasts a purity level of 99.999%, as highlighted in Fig. S19. This level of purity underscores the potential of this technology to produce high-quality hydrogen suitable for various applications, further enhancing its appeal in the realm of clean energy production. Furthermore, when we analyze the performance of our electrolyzer, we observe notable advancements in comparison to recently published results, as depicted in Fig. 7e and detailed in Table S4.

Moreover, we assessed electricity consumption for the production of 1 kg of H₂ using an industrial alkaline water electrolyzer at various current densities (300, 500, 600, and 1000 mA cm⁻²). The comprehensive calculations are outlined in the [supplementary information](#). As illustrated in Fig. 7f, the AEMWE demonstrates remarkable efficiency, requiring only 42.53, 43.86, 47.19, and 47.85 kWh of electricity at 300, 500, 600, and 1070 mA cm⁻², respectively, to generate 1 kg of H₂. These consumption values fall below the threshold established for industrial electrolyzers (48 kWh), underscoring a promising path toward achieving sustainable H₂ production within the realm of commercial water electrolysis. Lastly, we conducted a comprehensive assessment of

cell efficiency across a range of current densities, specifically at 300, 500, 600, and 1070 mA cm⁻² (with detailed calculations provided in the [supplementary information](#)). As depicted in [Fig. 7g](#), the cell efficiency demonstrates robust performance, registering at 78.14%, 76%, 73.77%, and 69.67% for the respective current densities. These results notably converge closely with the efficiency target established by the U.S. Department of Energy (DOE) for water electrolysis, with the target efficiency precisely set at 77%. This alignment underscores the promising potential of our system in meeting critical benchmarks for efficient water electrolysis.

3.4. Computational study

Computational methods offer an alternative approach to studying catalyst performance. By utilizing density functional theory (DFT), we can model the structure of the NiCoFeSe catalysts based on experimental data, as shown in [Fig. 8a](#), FeSe ([Fig.S15](#)), CoFeSe ([Fig.S16](#)), NiFeSe ([Fig.S17](#)). In this study, we employ DFT to investigate the electronic structure properties by calculating the density of states (DOS).

The DOS, as presented in [Fig. 8b](#), unveils an intriguing trend: the introduction of Ni and Co doping in FeSe results in a noticeable augmentation of its DOS. This augmentation is particularly pronounced in NiCoFeSe, which demonstrates the highest DOS near the Fermi level when compared to FeSe, CoFeSe, and NiFeSe. This heightened DOS in NiCoFeSe strongly implies a substantial charge transfer within the material. To delve deeper into these findings, we conducted an in-depth examination of Gibbs free energies through DFT analysis. It is well-established that the kinetics of the HER are intricately linked to the Gibbs free energy ($\Delta G H^*$), particularly when it approaches values close to zero. In the case of FeSe, the presence of an active site associated with Fe contributes to achieving its activity. However, the introduction of Co dopants adsorbs various intermediates during HER processes, and this effect is further enhanced with the addition of Ni dopants, given their respective active sites [[64,65](#)]. As a result, our findings underscore that

NiCoFeSe boasts a $\Delta G H^*$ value of 0.6 eV, which is remarkably close to zero in comparison to FeSe, CoFeSe, and NiFeSe. The HER efficiency can be attributed to the interplay between Co, Fe and Ni effectively altering the electronic properties of the electrocatalyst. The introduction of Co, and Ni introduces supplementary active sites within the NiCoFeSe catalyst, thereby decreasing the energy required for water dissociation and enhancing the adsorption affinity for H⁺, consequently bolstering the HER performance of NiCoFeSe. This finding strongly suggests that NiCoFeSe is well-suited for hydrogen adsorption, as illustrated in [Fig. 8c](#). When considering the Gibbs free energy in the context of the OER, it becomes evident that the stepwise process of water oxidation plays a pivotal role. The transition from O^{*} to OOH^{*} stands out as a critical step in controlling this process. Transition metals like Ni and Co are particularly well-suited to attract intermediates that facilitate the production of oxygen [[66,67](#)]. As a consequence, the introduction of Co and Ni doping has rendered FeSe a more favorable candidate for OER. [Fig. 8d](#) showcases the theoretical overpotential of NiCoFeSe (0.9 V), which is notably lower than that of FeSe, CoFeSe, and NiFeSe, indicating its enhanced performance in the OER. The reduced theoretical overpotential value suggests that the doped Co and Ni material exhibits a robust affinity for OOH^{*}, leading to enhanced performance in the OER process. Consequently, the incorporation of Ni and Co effectively fine-tunes the electronic structure of NiCoFeSe, ultimately optimizing its ability to adsorb various intermediates during OER processes. Through computational methods, we have examined the performance of the catalysts. Our results demonstrate that NiCoFeSe exhibits a higher density of states near the Fermi level, suggesting sufficient charge transfer. Additionally, NiCoFeSe displays a lower Gibbs free energy for both HER and OER, indicating favorable kinetics for hydrogen adsorption and improved performance in the OER.

4. Conclusions

In conclusion, we successfully synthesized a MOF-based Ni and Co-

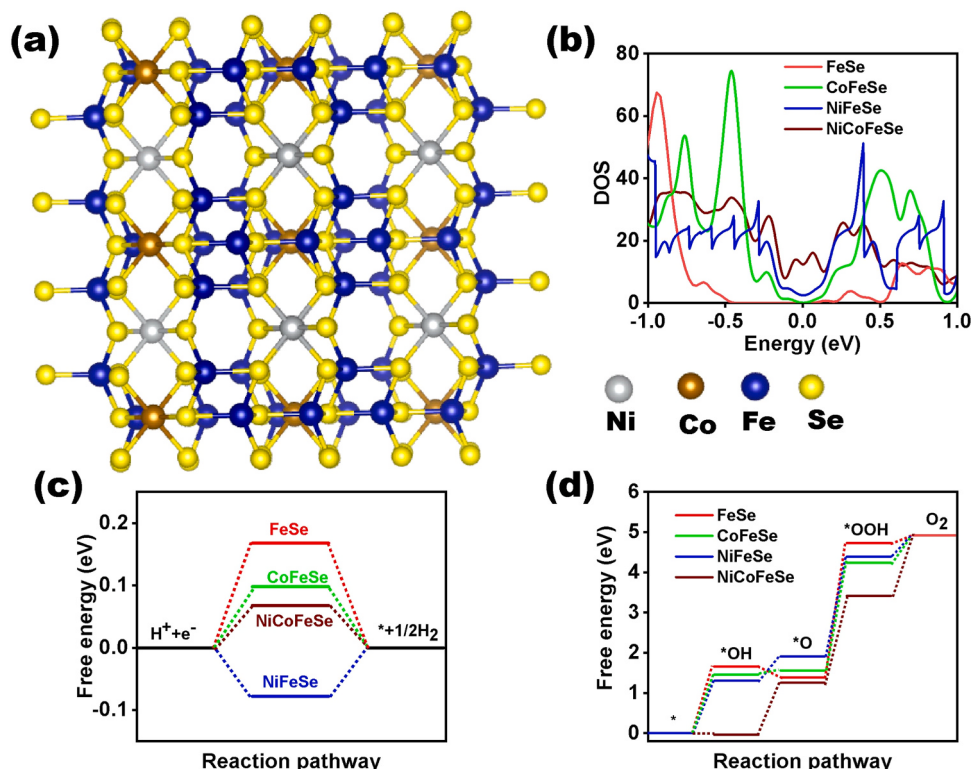


Fig. 8. (a) Depicts the atomic structure model of NiCoFeSe, (b) Displays the Density of States (DOS) values, (c) Compares the changes in Gibbs free energy ($\Delta G H^*$), (d) Illustrates the Gibbs free-energy changes.

doped iron selenide (NiCoFeSe) hexagonal nanorod catalyst for efficient overall water splitting. The synthesis process involved a facile and scalable hydrothermal method using a MOF precursor, which allowed for the controlled formation of NiCoFeSe nanorods with a well-defined hexagonal morphology. The incorporation of Ni and Co dopants enhanced the catalytic activity of the NiCoFeSe catalyst. Through extensive characterization techniques, we confirmed the successful synthesis of NiCoFeSe hexagonal nanorods with a homogeneous distribution. This segregation of Ni and Co in the iron selenide structure has significant implications for the catalytic performance of NiCoFeSe. The NiCoFeSe catalyst has demonstrated exceptional performance across various electrochemical reactions, including the HER, OER, and UOR. The NiCoFeSe remarkable attributes are characterized by impressively low overpotentials of 220 mV and 275 mV for HER, 230 mV and 330 mV for OER, and 210 mV and 300 mV for UOR at current densities of 50 and 100 mA cm^{-2} , respectively with low activation energy of 16.23 kJ mol^{-1} . Moreover, this versatile catalyst has been successfully applied in the fabrication of wireless flexible and rigid photovoltaic-electrochemical devices, achieving an impressive solar-to-hydrogen efficiency of 11.1%. Additionally, its utilization in an anion exchange membrane water electrolyzer resulted in remarkable outcomes, with a current density of 1.07 A cm^{-2} at 1.85 V, a cell efficiency of 69.67%, and an energy consumption of 47.85 kWh for the production of 1 kg of hydrogen. These findings underscore the potential of NiCoFeSe as a catalyst with broad applicability and high efficiency in renewable energy conversion. The stability and durability of the NiCoFeSe catalyst were also demonstrated over prolonged time of 200 h. These findings highlight the potential of MOF-based NiCoFeSe hexagonal nanorods as efficient catalysts for sustainable water splitting. The development of such catalysts offers promising prospects for achieving efficient and cost-effective hydrogen production through overall water splitting. The use of MOF-based catalysts provides a versatile and tunable platform for further advancements in electrocatalysis and contributes to the development of clean and renewable energy technologies.

CRediT authorship contribution statement

Mikiyas Mekete Meshesha: Conceptualization, Methodology, Software, Data curation, Writing – original draft, Revise, Writing – review & editing, **Debabrata Chanda:** Conceptualization, Revise, Writing – review & editing, Resources, Validation, Methodology. **Ranjith Balu, Seok Gwon Jang, Shahbaz Ahmed:** Resources, Validation, Methodology, **Bee Lyong Yang:** Conceptualization, Revise, Funding, Writing – review & editing, Supervision.

Declaration of Competing Interest

The authors declare that they have no known competing financial interests or personal relationships that could have appeared to influence the work reported in this paper.

Data Availability

Data will be made available on request.

Acknowledgment

This work was supported by Ministry of Science and ICT, Bidirectional Technology Excavation Support Project No., 1711177969 and 1711178804 and Korea Institute of Startup & Entrepreneurship Development, Preliminary Start-up Package support Project No. 10438934.

Appendix A. Supporting information

Supplementary data associated with this article can be found in the online version at [doi:10.1016/j.apcatb.2023.123635](https://doi.org/10.1016/j.apcatb.2023.123635).

References

- [1] S. Ibraheem, G. Yasin, A. Kumar, M.A. Mushtaq, S. Ibrahim, R. Iqbal, M. Tabish, S. Ali, A. Saad, Iron-cation-coordinated cobalt-bridged-selenides nanorods for highly efficient photo/electrochemical water splitting, *Appl. Catal. B: Environ.* 304 (2022), 120987.
- [2] W. Bao, J. Yang, W. Yan, Y. Tang, Z. Yang, Y. Zhao, G. Wang, S. Yang, F. Yu, Rapid in situ synthesis of sulfur-doped transition-metal oxyhydroxides by room temperature impregnation for advanced electrocatalytic splitting water, *J. Power Sources* 580 (2023), 233307.
- [3] S. Lv, Y. Deng, Q. Liu, Z. Fu, X. Liu, M. Wang, Z. Xiao, B. Li, L. Wang, Carbon-quantum-dots-involved Fe/Co/Ni phosphide open nanotubes for high effective seawater electrocatalytic decomposition, *Appl. Catal. B: Environ.* 326 (2023), 122403.
- [4] K. Chen, Y.H. Cao, S. Yadav, G.C. Kim, Z. Han, W. Wang, W.J. Zhang, V. Dao, I. H. Lee, Electronic structure reconfiguration of nickel-cobalt layered double hydroxide nanoflakes via engineered heteroatom and oxygen-vacancies defect for efficient electrochemical water splitting, *Chem. Eng. J.* 463 (2023), 142396.
- [5] J. Gautam, Y. Liu, J. Gu, Z. Ma, J. Zha, B. Dahal, L.N. Zhang, A.N. Chishti, L. Ni, G. Diao, Y. Wei, Fabrication of polyoxometalate anchored zinc cobalt sulfide nanowires as a remarkable bifunctional electrocatalyst for overall water splitting, *Adv. Funct. Mater.* 31 (2021) 2106147.
- [6] H. Gao, J. Liu, Z. Zhang, Y. Lu, R. Chen, Y.C. Huang, C. Xie, M. Qiu, T. Wu, J. Wang, Y. Jiang, C.L. Dong, Z. Kong, S. Wang, Electrochemical etching induced high-valence cobalt with defects site for boosting electrochemical water splitting, *Chem. Eng. J.* 463 (2023), 142224.
- [7] V.H. Hoa, M. Austeria, H.T. Dao, M. Mai, D.H. Kim, Dual-phase cobalt phosphide/phosphate hybrid interactions via iridium nanocluster interfacial engineering toward efficient overall seawater splitting, *Appl. Catal. B: Environ.* 327 (2023), 122467.
- [8] M. Wang, X. Zheng, Y. Li, Z. Zou, Y. Ling, Q. Wang, KCl-assisted rapid and low-cost synthesis of antiperovskite $(\text{Fe}_{1-x}\text{Cu}_x)_4\text{N}$ anchored on Cu_2O nanosheets for highly efficient electrochemical overall water splitting, *Chem. Eng. J.* 460 (2023), 141854.
- [9] D.T. Tran, V.H. Hoa, H.T. Le, N.H. Kim, J.H. Lee, hierarchically porous nickel-cobalt phosphide nanoneedle arrays loaded micro-carbon spheres as an advanced electrocatalyst for overall water splitting application, *Appl. Catal. B: Environ.* 253 (2019) 235–245.
- [10] Y. Wu, Y. Yi, Z. Sun, H. Sun, T. Guo, M. Zhang, L. Cui, K. Jiang, Y. Peng, J. Sun, Bimetallic Fe-Ni phosphide carved nanoframes toward efficient overall water splitting and potassium-ion storage, *Chem. Eng. J.* 390 (2020), 124515.
- [11] V. Vij, S. Sultan, A.M. Harzandi, A. Meena, J.N. Tiwari, W.G. Lee, T. Yoon, K. S. Kim, Nickel-based electrocatalysts for energy related applications: oxygen reduction, oxygen evolution, and hydrogen evolution reactions, *ACS Catal.* 7 (2017) 7196–7225.
- [12] W.Z. Chen, P.Y. Liu, L. Zhang, Y. Liu, Z. Liu, J. He, Y.Q. Wang, High-efficient and durable overall water splitting performance by interfacial engineering of Fe-doped urchin-like $\text{Ni}_2\text{P}/\text{Ni}_3\text{S}_2$ heterostructure, *Chem. Eng. J.* 424 (2021), 130434.
- [13] M.Q. Yang, J. Wang, H. Wu, G.W. Ho, Noble Metal-free nanocatalysts with vacancies for electrochemical water splitting, *Small* 14 (2018) 1703323.
- [14] Y. Zhang, H. Guo, X. Li, J. Du, W. Ren, R. Song, A 3D multi-interface structure of coral-like Fe-Mo-S/ $\text{Ni}_3\text{S}_2@\text{NF}$ using for high-efficiency and stable overall water
- [16] J. Gautam, K. Kannan, M. M. Meshesha, B. Dahal, S. Subedi, L. Ni, Y. Wei, B.L. Yang, Heterostructure of polyoxometalate/zinc-iron-oxide nanoplates as an outstanding bifunctional electrocatalyst for the hydrogen and oxygen evolution reaction, *Journal of Colloid and Interface Science*, 618 (2022) 419–430.
- [15] D. Chanda, K. Kannan, J. Gautam, M.M. Meshesha, S.G. Jang, V.A. Dinh, B.L. Yang, Effect of the interfacial electronic coupling of nickel-iron sulfide nanosheets with layer Ti3C2 MXenes as efficient bifunctional electrocatalysts for anion exchange membrane water electrolysis, *Appl. Catal. B: Environ.* 321 (2023), 122039.
- [16] K. Kannan, D. Chanda, J. Gautam, M.M. Meshesha, S.G. Jang, B.L. Yang, Facial synthesis of p-p heterojunction composites: Evaluation of their electrochemical properties with photovoltaics-electrolyzer water splitting using two-electrode system, *Int. J. Hydrol. Energy* 48 (2023) 13814–13826.
- [17] M.M. Meshesha, K. Kannan, D. Chanda, J. Gautam, S.G. Jang, B.L. Yang, Remarkable photoelectrochemical activity of titanium dioxide nanorod arrays sensitized with transition metal sulfide nanoparticles for solar hydrogen production, *Mater. Today Chem.* 26 (2022), 101216.
- [18] K. Kannan, J. Gautam, D. Chanda, M.M. Meshesha, S.G. Jang, B.L. Yang, Two dimensional MAX supported copper oxide/nickel Oxide/MAX as an efficient and novel photocatalyst for hydrogen evolution, *Int. J. Hydrol. Energy* 48 (2023) 7273–7283.
- [19] J. Gautam, D. Chanda, M.M. Meshesha, S.G. Jang, B.L. Yang, Heterointerface of vanadium telluride and zinc iron telluride nanosheets for highly efficient hydrogen production via water and urea electrolysis, *Chem. Eng. J.* 467 (2023), 143535.
- [20] M.M. Meshesha, J. Gautam, D. Chanda, K. Kannan, S.G. Jang, B.L. Yang, Effect of reaction temperature on morphology and photoelectrochemical performance of titanium dioxide, *Mater. Lett.* 329 (2022), 133176.
- [21] L. Han, S. Dong, E. Wang, Transition metal (Co, Ni, and Fe) based electrocatalysts for the water oxidation reaction, *Adv. Mater.* 28 (2016) 9266–9291.
- [22] M.M. Meshesha, et, all, Enhancing the electrochemical activity of zinc cobalt sulfide via heterojunction with MoS_2 metal phase for overall water splitting, *Journal of Colloid and Interface Science*, 652,2023, 272–284 splitting, *Chemical Engineering Journal*, 404 (2021) 126483.

[23] M.M. Meshesha, D. Chanda, S.G. Jang, B.L. Yang, Enhancing cobalt-based bimetallic selenide performance for urea and water electrolysis through interface engineering, *Chem. Eng. J.* 474 (2023), 145708.

[24] D. Chanda, H. Kwon, M.M. Meshesha, J.S. Gwon, M. Ju, K. Kim, B.L. Yang, modulating interfacial electronic coupling of copper-mediated NiFe layered double hydroxide nanoprisms via structural engineering for efficient OER in wireless photovoltaic-coupled and anion exchange membrane water electrolysis, *Appl. Catal. B: Environ.* 340 (2024), 123187.

[25] Shuang Yang, Ji-Yu Zhu, Xiao-Nan Chen, Meng-Jie Huang, Sheng-Hao Cai, Ji-Yuan Han, Ji-Sen Li, Self-supported bimetallic phosphides with artificial heterointerfaces for enhanced electrochemical water splitting, *Appl. Catal. B: Environ.* Volume 304 (2022), 120914.

[26] Sheng-Hao Cai, Xiao-Nan Chen, Meng-Jie Huang, Ji-Yuan Han, Yu-Wei Zhou, Ji-Sen Li, Interfacial engineering of nickel/iron/ruthenium phosphides for efficient overall water splitting powered by solar energy, *J. Mater. Chem. A* 10 (2022) 772–778.

[27] Ji-Sen Li, Jia-Yi Li, Meng-Jie Huang, Ling-Xin Kong, Zexing Wu, Anchoring RuxP on 3D hollow graphene nanospheres as efficient and pH-universal electrocatalysts for the hydrogen evolution reaction, *Carbon* 161 (2020) 44–50.

[28] Ji-Sen Li, Shuai Zhang, Jing-Quan Sha, Hao Wang, Ming-Zhu Liu, Ling-Xin Kong, Guo-Dong Liu, Confined molybdenum phosphide in P-doped porous carbon as efficient electrocatalysts for hydrogen evolution, *ACS Appl. Mater. Interfaces* 10 (20) (2018) 17140–17146.

[29] X. Xia, L. Wang, N. Sui, V.L. Colvin, William W. Yu, Recent progress in transition metal selenide electrocatalysts for water splitting, *Nanoscale* 12 (2020) 12249–12262.

[30] D. Chen, R. Yu, D. Wu, H. Zhao, P. Wang, J. Zhu, P. Ji, Z. Pu, L. Chen, J. Yu, S. Mu, Anion-modulated molybdenum oxide enclosed ruthenium nano-capsules with almost the same water splitting capability in acidic and alkaline media, *Nano Energy* 100 (2022), 107445.

[31] Y. Zhang, J. Fu, H. Zhao, R. Jiang, F. Tian, R. Zhang, Tremella-like $\text{Ni}_3\text{S}_2/\text{MnS}$ with ultrathin nanosheets and abundant oxygen vacancies directly used for high speed overall water splitting, *Appl. Catal. B: Environ.* 257 (2019), 117899.

[32] X. Meng, Z. Li, Y. Liu, Z. Wang, P. Wang, Z. Zheng, Y. Dai, B. Huang, H. Cheng, J. H. He, Enabling unassisted solar water splitting with concurrent high efficiency and stability by robust earth-abundant bifunctional electrocatalysts, *Nano Energy* 109 (2023), 108296.

[33] L. Xu, F.T. Zhang, J.H. Chen, X.Z. Fu, R. Sun, C.P. Wong, Amorphous NiFe nanotube arrays bifunctional electrocatalysts for efficient electrochemical overall water splitting, *ACS Appl. Energy Mater.* 3 (2018) 1210–1217.

[34] J. Yu, J. Li, C.Y. Xu, Q. Li, Q. Liu, J. Liu, R. Chen, J. Zhu, J. Wang, Modulating the d-band centers by coordination environment regulation of single-atom Ni on porous carbon fibers for overall water splitting, *Nano Energy* 98 (2022), 107266.

[35] F. Zhang, Y. Ge, H. Chu, P. Dong, R. Baines, Y. Pei, M. Ye, J. Shen, Dual-Functional starfish-like P-doped Co–Ni–S nanosheets supported on nickel foam with enhanced electrochemical performance and excellent stability for overall water splitting, *ACS Appl. Mater. Interfaces* 8 (2018) 7087–7095.

[36] M. Chen, D. Liu, B. Zi, Y. Chen, D. Liu, X. Du, F. Li, P. Zhou, Y. Ke, J. Li, K.H. Lo, C. T. Kwok, W.F. Ip, S. Chen, S. Wang, Q. Liu, H. Pan, Remarkable synergistic effect in cobalt-iron nitride/allyl nanosheets for robust electrochemical water splitting, *J. Energy Chem.* 65 (2022) 405–414.

[37] F.O. Boakye, Y. Li, K.A. Owusu, I.S. Amiiniu, Y. Cheng, H. Zhang, One-step synthesis of heterostructured cobalt-iron selenide as bifunctional catalyst for overall water splitting, *Mater. Chem. Phys.* 275 (2022), 125201.

[38] M. Yu, J. Zheng, M. Guo, La-doped NiFe-LDH coupled with hierarchical vertically aligned MXene frameworks for efficient overall water splitting, *J. Energy Chem.* 70 (2022) 472–479.

[39] S. Shit, S. Chhetri, W. Jang, N.C. Murmu, H. Koo, P. Samanta, T. Kuila, Cobalt sulfide/nickel sulfide heterostructure directly grown on nickel foam: an efficient and durable electrocatalyst for overall water splitting application, *ACS Appl. Mater. Interfaces* 10 (2018) 27712–27722.

[40] H. Su, S. Song, S. Li, Y. Gao, L. Ge, W. Song, T. Ma, J. Liu, High-valent bimetal $\text{Ni}_3\text{S}_2/\text{Co}_3\text{S}_4$ induced by Cu doping for bifunctional electrocatalytic water splitting, *Appl. Catal. B: Environ.* 293 (2021), 120225.

[41] K. Nejati, A.R. Akbari, S. Davari, K.A. Zeynali, Z. Rezvani, Zn–Fe-layered double hydroxide intercalated with vanadate and molybdate anions for electrocatalytic water oxidation, *N. J. Chem.* 42 (2018) 2889–2895.

[42] L.M. Cao, J. Zhang, L.W. Ding, Z.Y. Du, C.T. He, Metal-organic frameworks derived transition metal phosphides for electrocatalytic water splitting, *J. Energy Chem.* 68 (2022) 494–520.

[43] Z. Zang, X. Wang, X. Li, Q. Zhao, L. Li, X. Yang, X. Yu, X. Zhang, Z. Lu, Co_9S_8 nanosheet coupled Cu_2S nanorod heterostructure as efficient catalyst for overall water splitting, *ACS Appl. Mater. Interfaces* 13 (2021) 9865–9874.

[44] K. Zeng, Y. Li, M. Tian, C. Wei, J. Yan, M.H. Rummeli, P. Strasser, R. Yang, Molybdenum-leaching induced rapid surface reconstruction of amorphous/crystalline heterostructured trimetal oxides pre-catalyst for efficient water splitting and Zn-air batteries, *Energy Storage Mater.* 60 (2023), 102806.

[45] G. Rajeshkhan, E. Umeshbabu, P. Justin, G.R. Ranga, Spinel ZnCo_2O_4 nanosheets as carbon and binder free electrode material for energy storage and electroreduction of H_2O_2 , *J. Alloy. Compd.* 696 (2017) 947–955.

[46] R. Li, Z. Hu, X. Shao, P. Cheng, S. Li, W. Yu, W. Lin, D. Yuan, Large scale synthesis of NiCo layered double hydroxides for superior asymmetric electrochemical capacitor, *Sci. Rep.* 6 (2016) 18737.

[47] G. Rajeshkhan, T.I. Singh, N.H. Kim, J.H. Lee, Remarkable bifunctional oxygen and hydrogen evolution electrocatalytic activities with trace-level Fe doping in Ni- and Co layered double hydroxides for overall water-splitting, *ACS Appl. Mater. Interfaces* 10 (2018) 42453–42468.

[48] G. Rajeshkhan, S. Kandula, K.R. Shrestha, N.H. Kim, J.H. Lee, A new class of $\text{Zn}_{1-x}\text{Fe}_x$ oxyselenide and $\text{Zn}_{1-x}\text{Fe}_x\text{-LDH}$ nanostructured material with remarkable bifunctional oxygen and hydrogen evolution electrocatalytic activities for overall water splitting, *Small* 14 (2018) 1803638.

[49] X. Zhang, H. Fan, J. Yuan, J. Tian, Y. Wang, C. Lu, H. Han, W. Sun, General approach to produce nanostructured binary transition metal selenides as high-performance sodium ion battery anodes, *Nano-Micro Small* 16 (2019) 1901995.

[50] Chunyan Zhang, Nianqiao Qin, An Pan, Jun Yuan, Qianqian Liu, Jiaqing Ren, Zhong-hua Xue, Mudassar Iqbal, Yan Tian, Fei Ke, Hollow Fe_2O_3 nanotubes derived from metal-organic framework for enhanced lithium storage and dye adsorption, *J. Porous Mater.* 28, 673–681.

[51] Wen-Tao Xu, Lin Ma, Fei Ke, Fu-Min Peng, Geng-Sheng Xu, Yu-Hua Shen, Jun-Fa Zhu, Ling-Guang Qiu, Yu-Peng Yuan, Metal-organic frameworks MIL-88A hexagonal microrods as a new photocatalyst for efficient decolorization of methylene blue dye, *Dalton Trans.* 43 (2014) 3792–3798.

[52] D. Wei, J. Liang, Y. Zhu, L. Hu, K. Zhang, J. Zhang, Z. Yuan, Y. Qian, Layer structured $\alpha\text{-FeSe}$: a potential anode material for lithium storage, *Electrochem. Commun.* 38 (2014) 124–127.

[53] H. Gong, Q. Liu, C. Huang, NiSe as an effective co-catalyst coupled with TiO_2 for enhanced photocatalytic hydrogen evolution, *Int. J. Hydrol. Energy* 44 (2019) 4821–4831.

[54] H. Gong, Q. Liu, C. Huang, NiSe as an effective co-catalyst coupled with TiO_2 for enhanced photocatalytic hydrogen evolution, *Int. J. Hydrol. Energy* 44 (2019) 4821–4831.

[55] A. Sun, Y. Qiu, Z. Wang, L. Cui, H. Xu, X. Zheng, J. Xu, J. Liu, Interface engineering on super-hydrophilic amorphous/crystalline NiFe-based hydroxide/selenide heterostructure nanoflowers for accelerated industrial overall water splitting at high current density, *J. Colloid Interface Sci.* 650 (2023) 573–581.

[56] L. Chen, Y.F. Yuan, M. Zhu, S.M. Yin, P.F. Du, C.L. Mo, Hierarchical hollow superstructure cobalt selenide bird nests for high-performance lithium storage, *J. Colloid Interface Sci.* 627 (2022) 449–458.

[57] Y. Jiang, B. Cai, R. Xiangyu Xu, H. Guo, X. Jin, Z. Chen, J. Xu, G. Liu, One-step electrodeposition preparation of NiCoSe_2 @carbon cloth as a flexible supercapacitor electrode material, *N. J. Chem.* 47 (2023) 12649–12657.

[58] H. Wang, Y. Yan, W. Zhang, S. Sun, S. Yao, Preparation of $\text{Co}(\text{OH})_2@\text{NiFe}/\text{NF}$ bifunctional electrocatalyst by electrodeposition for efficient water splitting, *J. Solid State Chem.* 323 (2023), 124048.

[59] C. Gong, L. Zhao, D. Li, X. He, H. Chen, X. Du, D. Wang, W. Fang, X. Zeng, W. Li, In-situ interfacial engineering of $\text{Co}(\text{OH})_2/\text{Fe}_2\text{Se}_3$ nanosheets to boost electrocatalytic water splitting, *Chem. Eng. J.* 466 (2023), 143124.

[60] W. Yaseen, N. Ullah, M. Xie, B.A. Yusuf, Y. Xu, C. Tong, J. Xie, Ni-Fe-Co based mixed metal/metal-oxides nanoparticles encapsulated in ultrathin carbon nanosheets: a bifunctional electrocatalyst for overall water splitting, *Surf. Interfaces* 26 (2021), 101361.

[61] P. Zuo, X. Ji, J. Lu, Y. Chai, W. Jiao, R. Wang, N. P co-doped Ni/Mo-based multicomponent electrocatalysts in situ decorated on Ni foam for overall water splitting, *J. Colloid Interface Sci.* 645 (2023) 895–905.

[62] I.P. Liu, H. Teng, Y.L. Lee, highly electrocatalytic carbon black/copper sulfide composite counter electrodes fabricated by a facile method for quantum-dot-sensitized solar cells, *J. Mater. Chem. A* 5 (2017) 23146–23157.

[63] M. García-Mota, M. Bajdich, V. Viswanathan, A. Vojvodic, A.T. Bell, J.K. Nørskov, Importance of correlation in determining electrocatalytic oxygen evolution activity on cobalt oxides, *J. Phys. Chem. C* 116 (2012) 21077–21082.

[64] T. Yu, H. Chen, T. Hu, J. Feng, W. Xing, L. Tang, W. Tang, Recent advances in the applications of encapsulated transition-metal nanoparticles in advanced oxidation processes for degradation of organic pollutants: a critical review, *Appl. Catal. B: Environ.* 342 (2024), 123401.

[65] X. Yan, C. Zhang, J. Hu, Y. Zhou, Z. Lv, Immobilization of Co nanoparticles into N-doped carbon nanotube on g-C₃N₄ via coordination-polymerization integrated strategy for efficient H_2 evolution reaction at all pH values, *Appl. Catal. B: Environ.* 342 (2024), 123354.

[66] H. Yu, W. Wang, Q. Mao, K. Deng, Z. Wang, Y. Xu, X. Li, H. Wang, L. Wang, Pt single atom captured by oxygen vacancy-rich NiCo layered double hydroxides for coupling hydrogen evolution with selective oxidation of glycerol to formate, *Appl. Catal. B: Environ.* 330 (2023), 122617.

[67] Z. Zheng, D. Wu, L. Chen, S. Chen, H. Wan, G. Chen, N. Zhang, X. Liu, R. Ma, Collaborative optimization of thermodynamic and kinetic for Ni-based hydroxides in electrocatalytic urea oxidation reaction, *Appl. Catal. B: Environ.* Volume 340 (2024), 123214.